LAWRENCE
LIVERMORE
NATIONAL
LABORATORY

UCRL-JRNL-210862

# Direct Observations of the (Alpha to Gamma) Transformation at Different Input Powers in the Heat Affected Zone of 1045 C-Mn Steel Arc Welds Observed by Spatially Resolved X-Ray Diffraction

T. A. Palmer, J. W. Elmer

March 25, 2005

Metallurgical and Materials Transactions A

## Disclaimer

UCRL-JRNL-210862

# Direct Observations of the α→γ Transformation at Different Input Powers in the Heat Affected Zone of 1045 C-Mn Steel Arc Welds Observed by Spatially Resolved X-Ray Diffraction

T.A. Palmer and J.W. Elmer

Lawrence Livermore National Laboratory, Livermore, CA 94550, United States

ABSTRACT

Spatially Resolved X-Ray Diffraction (SRXRD) experiments have been performed during Gas Tungsten Arc (GTA) welding of AISI 1045 C-Mn steel at input powers ranging from 1000 W to 3750 W. In situ diffraction patterns taken at discreet locations across the width of the heat affected zone (HAZ) near the peak of the heating cycle in each weld show regions containing austenite (γ), ferrite and austenite (α+γ), and ferrite (α). Changes in input power have a demonstrated effect on the resulting sizes of these regions. The largest effect is on the γ phase region, which nearly triples in width with increasing input power, while the width of the surrounding two phase α+γ region remains relatively constant. An analysis of the diffraction patterns obtained across this range of locations allows the formation of austenite from the base metal microstructure to be monitored. After the completion of the α→γ transformation, a splitting of the austenite peaks is observed at temperatures between approximately 860ºC and 1290ºC. This splitting in the austenite peaks results from the dissolution of cementite laths originally present in the base metal pearlite, which remain after the completion of the α→γ transformation, and represents the formation of a second more highly alloyed austenite constituent. With increasing temperatures, carbon, originally present in the cementite laths, diffuses from the second newly formed austenite constituent to the original austenite constituent. Eventually, a homogenous austenitic microstructure is produced at temperatures of approximately 1300ºC and above, depending on the weld input power.

## Introduction

Structural steels and other common commercial alloys undergo multiple thermal and mechanical treatments in order to form a desired microstructure. During welding, these carefully prepared microstructures are significantly altered by the rapid heating, melting, and cooling characteristic of this process. For example, the Heat Affected Zone (HAZ) in a common C-Mn steel weld displays significant variations from the desired equiaxed ferrite ($\alpha$)/pearlite($\alpha$+$Fe_3C$) base metal microstructure. These unique HAZ microstructural features are created during heating as the ferrite and pearlite in the base metal are transformed to austenite ($\gamma$), making the $\alpha \rightarrow \gamma$ transformation during heating of interest.

The formation of austenite from microstructures containing both pearlite and ferrite at intercritical annealing temperatures, defined as being between the A1 and A3 temperatures, has been extensively investigated.[1-9] Based on these previous investigations, the nucleation and growth of austenite is believed to occur over a series of steps. During heating, austenite first nucleates at ferrite($\alpha$)/pearlite interfaces and rapidly grows into the pearlite, which is rapidly consumed. A high carbon concentration austenite phase is formed at this point, but the remaining low carbon allotriomorphic ferrite, which is initially present along the prior austenite grain boundaries, remains untransformed. With increasing time and temperature, the remaining ferrite is transformed into austenite. Once the transformation of the ferrite/pearlite microstructure to austenite reaches completion, the carbon redistributes, and the austenite grains grow.

Other models note that the dissolution of cementite ($Fe_3C$) in the pearlite colonies is an important component in the transformation sequence.[10-12] In these models, local equilibrium is assumed at the austenite/cementite and ferrite/austenite boundaries as the $\alpha \rightarrow \gamma$ transformation proceeds to completion. The dissolution of the cementite present in the pearlite colonies, though, does not necessarily coincide with the disappearance of ferrite at the completion of the $\alpha \rightarrow \gamma$ transformation.[8,13-14] Undissolved cementite has been observed in a range of alloys after intercritical annealing in the $\alpha+\gamma$ phase region and with annealing above the A3 temperature. In many cases, extended annealing times, on the order of several hundred seconds, are required for the complete dissolution of these carbides.[8]

During welding, though, rapid continuous heating occurs at locations throughout the weld Heat Affected Zone (HAZ). A range of peak temperatures are experienced across the width of the HAZ and determine the extent to which the base metal microstructure transforms to austenite

during heating. As a result, three discreet microstructural regions are typically observed in the HAZ of a common C-Mn steel weld. At locations closest to the fusion zone boundary, the peak temperatures are the highest, allowing the $\alpha \rightarrow \gamma$ transformation to proceed to completion and the resulting $\gamma$ grains to grow. The result is a coarse grain (CGHAZ) microstructural region with grains larger than those in the base metal. As the distance from the fusion zone increases, the peak temperatures decrease to levels closer to the $\alpha \rightarrow \gamma$ transformation temperature, resulting in a decreased size of the $\gamma$ grains during heating. These smaller $\gamma$ grains represent the transformed microstructure prior to grain growth and form a fine grain (FGHAZ) microstructural region with grains smaller than those in the base metal. With even greater distance, the peak temperatures are not high enough to drive the $\alpha \rightarrow \gamma$ transformation to completion, resulting in a partially transformed microstructure (PTHAZ) containing both transformed austenite and untransformed ferrite and pearlite.[15,16]

Conventional characterization techniques, such as metallography or dilatometry, are unable to directly monitor the $\alpha \rightarrow \gamma$ transformation at discreet locations in the HAZ during the weld heating cycle. However, Spatially Resolved X-Ray Diffraction (SRXRD) using high energy synchrotron radiation can provide this information through the *in-situ* monitoring of phase transformations in real time.[17] This technique has been used to study phase transformations occurring during the heating and cooling cycles present in the Gas Tungsten Arc (GTA) welding of commercially pure titanium, C-Mn steels, and stainless steels.[18-22] The resulting x-ray diffraction patterns can then be analyzed in order to determine the degree to which a phase transformation has progressed or to monitor changes in the characteristics of each phase.[22-25] Based on these results, the kinetics of the prominent phase transformations taking place in each materials system can be experimentally measured and the results applied to existing phase transformation models.[23-25]

In these previous SRXRD studies, a map of the phases present in the weld HAZ is constructed for a single set of welding conditions. Changes in the input power, though, can have demonstrated effects on both the size of the HAZ and the heating and cooling cycles experienced across its width. The effect of changes in the input power has been investigated in a Ti-6Al-4V alloy using SRXRD techniques.[26] Increasing input powers have measured effects on both the size of the $\beta$-Ti phase region and the kinetics of the $\alpha \rightarrow \beta$ phase transformation in the weld HAZ. No studies, though, have been performed to examine the effects of changes in the input power on

the size of the high temperature γ phase region or the kinetics of the α→γ phase transformation in the HAZ of C-Mn steels.

In this study, a series of seven GTA welds with input powers ranging from 1003 W to 3759 W have been made on an AISI 1045 C-Mn steel. During each weld, an SRXRD scan, beginning at a location near the weld pool center and proceeding outward to a distance of approximately 20 mm from the weld centerline, is made. This scan is made in line with the heat source in order to monitor the α→γ phase transformation near the peak of the heating cycle and extends from the liquid weld pool through the HAZ to the base metal. The resulting observations are then correlated with the calculated thermal cycles and the resulting HAZ microstructures. The progress of the α→γ phase transformation, to include the formation, growth, and homogenization of austenite, near the peak of the heating cycle is, thus, monitored. By examining welds made with different input powers, the effect of different heating cycles on the resulting HAZ microstructures can also be determined. Both SRXRD and Time Resolved X-Ray Diffraction (TRXRD) techniques are currently being used to examine the kinetics of the α→γ transformation in the weld HAZ of C-Mn steels with varying carbon concentrations.[20,23-25,27] The additional kinetic data provided by this study will be combined with similar results taken from experiments with other C-Mn steels in order to quantify the effects of varying carbon concentrations on the kinetics of the α→γ phase transformation during welding.

## **Experimental**:

### *Material and Welding*

A series of Gas Tungsten Arc (GTA) welds have been made on AISI 1045 C-Mn Steel (Fe-0.46 C-0.85 Mn-0.014 P-0.020 S-0.270 Si-0.01 Cu-0.02 Ni-0.11 Cr-0.010 Mo-0.027 Al-0.005 V-0.0030 N-0.001 Nb- 0.001 Sn) samples. These samples have been machined from 10.8 cm diameter forged bar stock into welding samples which are 10.2 cm in diameter and 7.6 cm in length. Figure 1(a) shows a typical example of this microstructure, which is revealed using a 2% Nital solution. The base metal microstructure of the AISI 1045 C-Mn steel contains pearlite ($\alpha+Fe_3C$) and allotriomorphic ferrite, which is the light etching phase that outlines the prior austenite grain boundaries. Inside the prior austenite grains, the microstructure consists of the darkly etched pearlitic colonies, which occupy the majority of the microstructure. Higher magnification images of the pearlitic regions and the regions containing allotriomorphic ferrite are

shown in Figures 1(b) and 1(c), respectively. Quantitative metallography was performed on this microstructure using Image Pro®, Ver. 4.1. Measurements made at several locations show that the microstructure contains 12% allotriomorphic ferrite and 88% pearlite. The prior austenite grain size of the base metal was measured to be 92.8 μm in diameter. In addition, the size of the allotriomorphic grain boundary ferrite phase was shown to be 15 μm to 20 μm wide on average, with some patches reaching widths of 30 μm or more.

Using ThermoCalc® and the TC Fe2000 database, a pseudo-binary phase diagram for this alloy has been constructed and is shown in Figure 2. The nominal carbon concentration for this alloy is indicated on the plot. Based on these calculations, the liquidus temperature for this alloy is 1494ºC, the solidus temperature is 1421ºC, the A3 temperature is 765ºC, and the A1 temperature is 711ºC. These temperatures represent the calculated equilibrium temperatures at which the primary phase transformations in this alloy occur. In particular, the A1 temperature corresponds to the temperature at which austenite first appears in the microstructure, and the A3 temperature corresponds with the temperature at which ferrite disappears and the microstructure is completely transformed to austenite.

A summary of the welding conditions for the range of input powers is given in Table 1. In order to change the input power for each weld, the arc current is varied. The welding process is monitored in real-time using an infrared (IR) camera (FLIR® SC1000). In the images produced by this camera, the weld bead displays a side-to-side motion, which is minimized by the pulsing of the welding current at a frequency of 300 Hz. During welding, the travel speed is maintained constant at a value of 0.6 mm/sec, and the stand-off distance between the tip of the welding electrode and the sample surface is also maintained constant at a distance of approximately 2.8 mm. All welds are made in an environmentally sealed chamber in order to avoid atmospheric contamination of the weld. The chamber is also back-filled with helium in order to aid in the passage of the synchrotron x-rays. More details pertaining to the welding portion of these experiments can be found in previous publications.[18-22]

*Spatially Resolved X-Ray Diffraction*

The SRXRD experiments are performed on the 31-pole wiggler beam line (BL 10-2)[28] at the Stanford Synchrotron Radiation Laboratory (SSRL) on the Stanford Positron-Electron Asymmetric Ring (SPEAR). In this setup, the synchrotron beam emerges from the wiggler and

is focused by a toroidal mirror to a size of approximately 1 mm high x 2 mm wide and monochromatized with a double Si(111) crystal. The focused beam then passes through a 260 μm tungsten pinhole to render a sub-millimeter beam on the sample at an incident angle of approximately 25˚. These portions of the experimental set-up are shown schematically in Figure 3. A photon energy of 12.0 keV ($\lambda$ = 0.1033 nm) has been chosen to maximize the number of observable diffraction peaks in the 2$\theta$ window and to ensure that the photon energy is high enough above the Fe K-edge (7.112 keV) and the Ni K-edge (8.332 keV), both of which are constituent elements in the sample, to minimize the K-fluorescence contribution from the sample. Further details regarding the experimental set-up are described in detail elsewhere.[18-26]

In each SRXRD run, approximately 100 diffraction patterns spaced 200 μm apart are gathered along a linear path beginning at the weld centerline and proceeding outward in a direction perpendicular to the direction of weld travel and in line with the welding electrode. Overall, a distance of nearly 20 mm from the weld centerline is examined. Each data point consists of a diffraction pattern recorded while the beam is at a fixed location. For each pattern, an integration time of 4 seconds is used while the bar is rotated under the torch at a constant speed. With a travel speed of 0.6 mm/sec, each SRXRD pattern is thus integrated over a distance of approximately 2.4 mm.

Two discreet sources of error contribute to the spatial accuracy of the SRXRD data: the accuracy of the location of the x-ray beam with respect to the weld centerline and the side-to-side motion of the weld pool at the solid/liquid interface. The x-ray beam position with respect to the weld centerline determines both the starting point for the SRXRD measurements and the resulting locations of the phases detected in the x-ray diffraction patterns. In order to adjust the electrode position to the desired starting position for the SRXRD measurements, x-ray sensitive photographic paper (Kodak Type 2167) is placed on the bar and the x–ray spot is imaged on the paper. When considering the accuracy of the scale used to determine this position, an uncertainty of ±0.25 mm in the starting location of the beam is present. The weld bead also displays a side-to-side motion, which is minimized by the use of a pulsed current in the welding process. Still, an additional uncertainty of ±0.25 mm is estimated in the actual location of the weld fusion line.

Variations in the measured weld pool width over the length of each weld also contribute another source of error. During welding, the weld width can vary by upwards of 0.5 mm from start to finish. In order to minimize the effects of these variations, SRXRD measurements are taken

beginning approximately 30 seconds after the start of welding. At this point, the greatest variations in the weld width, which occur at the beginning of the weld, have taken place and the weld has reached steady state. The reported weld width is the average of measurements taken at its beginning, middle, and end of the weld. This variation in the weld width contributes an additional uncertainty in the SRXRD position of approximately ±0.4 mm, which is the standard deviation of the weld width measurements.

Taken together, these sources of error result in an uncertainty of approximately ±0.9 mm in the position of a measurement. This potential error is reduced by noting the location of the first observed solid phase in each scan, which defines the fusion zone boundary. By matching the SRXRD results with the actual location of the fusion zone boundary, errors introduced by variations in the weld pool size and slight misplacements in the starting location for the SRXRD scan are removed, thus significantly decreasing the error introduced into the measurements to approximately ±0.25 mm.

Using the x-ray diffraction patterns gathered in each SRXRD run, the locations at which austenite, ferrite, or both are present in the weld HAZ at each input power are determined. In these diffraction patterns, three peaks representing the austenite phase, the fcc(111), fcc(200), and fcc(220) peaks, and an additional three peaks representing the ferrite phase, the bcc(110), bcc(200), and bcc(211) peaks, are observed across the length of each SRXRD scan. Along this one-dimensional scan, the locations of the primary phase regions, including the $\gamma$, $\alpha+\gamma$, and $\alpha$ phase regions, are identified and correlated with the location of the weld pool and important calculated isotherms.

An additional analysis of the individual Bragg peaks in each diffraction pattern is performed in order to extract thermal and microstructural properties of the phases present at each location. In addition to the peak position ($2\theta$ value), both the integrated intensity, which is the area measured under the peak, and the full width at half maximum (FWHM) values are measured. The position, width, and area of each peak are measured by fitting the experimental peak with one or more Gaussian peak profile functions and a linear background using an automated curve-fitting routine developed in Igor Pro®, Version 4.0. Shifts in the peak positions reflect expansions or contractions of the lattice parameters with either changes in temperature, composition, or strain. A broadening or narrowing of the peak is generally caused by changes in the micro-strain of the

individual phases and may be indications of mechanisms governing phase transformations. These analyses have been described in detail in previous works.[22,23]

During each SRXRD run, there are several diffraction patterns containing both ferrite (bcc) and austenite (fcc) peaks. Based on a comparison between the integrated intensities of the peaks present in each diffraction pattern, a conversion to volume fractions of austenite and ferrite can be made. Additional factors, such as the crystal structure and temperature, which affect the integrated intensity of each peak must also be taken into account, and these factors are discussed in detail in a standard x-ray diffraction reference [29]. A general methodology used to convert the raw integrated intensities into the relative volume fractions of austenite and ferrite has been used previously in an SRXRD study on AISI 1005 C-Mn steel and is discussed in detail elsewhere.[23] In these calculations, the effects of the crystal structure, the Lorentz polarization factor, and the temperature are considered. After these corrections are applied, the austenite volume fraction is calculated by dividing the sum of corrected austenite peak intensities by the sum of the corrected peak intensities in each diffraction pattern. The ferrite volume fraction is then determined by subtracting the austenite volume fraction from unity, since only two phases exist in the microstructure at these locations.

*Heat Transfer Modeling*

Knowledge of both the weld pool geometry and temperatures present across the span of the weldment is necessary to accurately map the phases present in the weldment. Since the direct measurement of these temperatures is difficult, calculations using complex mathematical models have been undertaken. The model used here has been tested extensively on a number of different materials systems under a variety of welding parameters by DebRoy and coworkers.[19,22,30-33] Only a cursory description is included below.

This thermo-fluids model is a three dimensional, heat transfer and fluid flow model, which numerically solves the equations of conservation of mass, momentum, and energy. These calculations are performed under steady-state conditions, using a coordinate system attached to and moving with the heat source. A Cartesian coordinate system is used in these calculations, which are performed on only half the workpiece because of the mirror symmetry of the weld pool, and a flat weld pool surface has been assumed. A computational domain of 76x43x46 grids encompassing a volume of 3.2 x 1.88 x 2.3 $cm^3$ is used in these calculations along with non-uniform

grid spacing. The boundary conditions used in these calculations are similar to those used in previous studies.[19,22,32-33]

A common set of material parameters has been used in each set of calculations for the different welding conditions. These values are summarized in Table 2.[34,35] For each input power, the material properties considered in the calculations are the same. In order to account for variations in the welding conditions which may arise with increases in the input power, the arc efficiency, arc radius, and preheat temperature have been varied in the model calculations. These values are summarized in Table 3 for each input power.

The calculated weld pool dimensions and selected isotherms are then compared with the experimental weld pool dimensions and the first appearance of austenite in the SRXRD results. Figure 4(a) shows the calculated thermal cycles for each input power over the range of each SRXRD scan, and Figure 4(b) shows an exploded view of these same thermal cycles in the vicinity of the A1 and A3 temperatures, where the nucleation of austenite from the base metal microstructure is expected. In general, the calculated thermal cycles are typical of those found in arc welds and are consistent with the experimentally measured weld dimensions, phase locations, and thermodynamic calculations for the welds studied here.

## Results and Discussion

### *Effects of Input power on Weld Geometry*

Changes in the input power have a measurable effect on the resulting weld pool dimensions and the size of the HAZ. In Figures 5(a-c), the width, depth, and aspect (depth/width) ratio for each weld are plotted as a function of the input power. The widths plotted in Figure 5(a) are the averages of measurements made on the top surface of each weld at various locations along the length of the weld. The weld depths plotted in Figure 5(b) are measured from a weld cross section taken from a location near the midpoint of the length of each weld. Both the weld width and depth increase by nearly a factor of 2.5 over the range of input powers. However, the aspect ratios remain constant at a value of approximately 0.6, which is a typical value for arc welds made in steel. Such a similarity in aspect ratios suggests that the fluid dynamics are similar in each case. These experimental weld dimensions are then compared with the values calculated using the 3D thermo-fluids model in Table 4. In this table, the experimental and calculated values for

the weld width, depth, and aspect ratio are listed for each input power. The calculated weld dimensions correspond very well with the measured values.

X-ray diffraction patterns are gathered at discreet locations along the length of each SRXRD scan. Examples of diffraction patterns taken from four locations in the SRXRD scan for the weld made at an input power of 1984 W are shown in Figures 6(a-d). The first diffraction pattern (Figure 6(a)) is taken at a location 3.2 mm from the weld centerline and displays no diffraction peaks, indicating the presence of liquid metal. As the distance from the weld centerline is increased, diffraction patterns containing various solid phases are observed. For example, at a location 5.4 mm (Figure 6(b)) from the weld centerline, austenite peaks are observed in the diffraction pattern. At a location 7.4 mm (Figure 6(c)) from the weld centerline, both ferrite and austenite peaks are observed. While at a location 11.6 mm (Figure 6(d)) from the weld centerline, only ferrite peaks are observed.

Within the austenite phase regions, the $\gamma$ peaks display a splitting behavior at each power input. An example of the splitting of a fcc(111) peak at a location 5.2 mm from the weld centerline for a weld made at an input power of 1984 W is shown in Figure 7. In this figure, the two peaks are separated by a $2\theta$ value of approximately 0.3º. Splitting is observed in all three austenite peaks present in the diffraction patterns obtained at locations which define the $\gamma$ phase region and occurs at temperatures between approximately 930ºC and 1240ºC, as shown in Table 5. The systematic nature of this peak splitting indicates that there is a distinct phenomenon occurring in the austenite phase. A more in-depth discussion of this peak splitting behavior is presented in a later section.

The locations of the $\gamma$, $\alpha+\gamma$, and $\alpha$ phase regions observed in the SRXRD scan made at a weld input power of 1984 W are shown Figure 8. Calculated isotherms for the liquidus, solidus, A3, and A1 temperatures, and the locations of the HAZ microstructural features observed in the post-weld metallography are also shown. In addition, the locations over which this splitting behavior in the austenite peaks in the $\gamma$ phase region is also indicated. The characteristics of this SRXRD scan are similar to those observed in the scans constructed for the other input powers.

The widths of the $\gamma$ and $\alpha+\gamma$ phase regions measured in each SRXRD run are plotted in Figure 9 as a function of the input power. These values are then compared with the calculated sizes of these phase regions, based on thermodynamic considerations. The calculated size of the $\gamma$

phase region is the distance between the calculated A3 and A4 isotherms, and the calculated size of the $\alpha+\gamma$ phase region is the distance between the calculated A1 and A3 isotherms.

Since the input power affects the resulting thermal profiles of each weld, as shown in Figure 4(a), corresponding changes in the size and locations of the individual phase regions are expected. Figure 9 confirms that both the experimental and calculated $\gamma$ phase and $\gamma$ peak splitting regions increase in size with increasing input power. The variations between the calculated and experimental sizes of the $\gamma$ phase region differ over the range of input powers investigated here. These differences are largest at the lower input powers where the temperature gradients for the weld input powers are highest. At the higher input powers, the experimental and calculated sizes of the $\gamma$ phase region are similar. The experimental and calculated sizes of the $\alpha+\gamma$ phase regions, though, remain fairly constant over the range of input powers, but the size of the experimental $\alpha+\gamma$ phase region is always higher than that determined using the thermo-fluid calculations.

*Correlating High-Temperature and Post-Weld Microstructures*

The SRXRD scan performed on each weld provides a snapshot of the phases present at or near the peak temperatures experienced at each HAZ location during the weld heating cycle. With the $\alpha\rightarrow\gamma$ transformation having proceeded to nearly its maximum extent, the resulting high-temperature microstructure provides a template for the microstructure formed during cooling. This microstructure can be observed in the post-weld metallography, as shown in Figure 10, which provides a complete metallographic view of the weld HAZ at an input power of 1984 W. In this figure, the three HAZ microstructural regions, namely the PTHAZ, FGHAZ, and CGHAZ, are identified. These microstructural features are also present in the welds made at the other input powers studied here but vary in size.

Moving from the base metal towards the fusion zone, a partially transformed region is encountered at the edge of the weld HAZ adjacent to the unaffected base metal. This region corresponds with the beginning of the $\alpha\rightarrow\gamma$ transformation. Temperatures in this region, though, do not reach sufficient levels for a long enough period of time during the heating cycle to allow the $\alpha\rightarrow\gamma$ transformation to reach completion. This region thus contains both transformed austenite and untransformed ferrite and pearlite. A closer view of this region is shown in Figure 11(a). Untransformed allotriomorphic ferrite, which originates in the base metal, is identified on the

micrograph. The remaining microstructure consists of fine-grained pearlite and allotriomorphic ferrite, which forms during cooling from the transformed austenite. Within the pearlitic regions, small regions of allotriomorphic ferrite are visible along apparent prior austenite grain boundaries. These prior austenite grains are much smaller in size than those observed in the base metal and are on the order of 5 to 10 μm in diameter.

At locations closer to the fusion zone boundary, the temperatures during the heating cycle rise to levels in excess of the A3 temperature, allowing the $\alpha \rightarrow \gamma$ transformation to reach completion. As a result, a completely austenitic high temperature microstructure is formed. However, these temperatures do not significantly exceed the A3 temperature and exist for rather short times, allowing nucleation and only limited growth of the $\gamma$ grains. A fine-grained austenitic microstructure is thus created as the new $\gamma$ grains nucleate and grow from the base metal grains. This microstructure later transforms to the fine grained ferritic and pearlitic microstructure shown in Figure 11(b) during weld cooling.

The region adjacent to the fusion zone boundary experiences temperatures during heating significantly higher than that required for the $\alpha \rightarrow \gamma$ transformation to proceed to completion. These temperatures also persist for much longer periods of time, allowing grain growth to proceed. This region exhibits measurable grain growth, which is displayed in Figure 11(c). In this figure, a large prior austenite grain is shown, with a combination of allotriomorphic and Widmanstätten ferrite present on the prior austenite grain boundaries. This prior austenite grain size appears to be in excess of 50 μm in diameter, thus displaying much greater austenite grain growth during heating than observed in the other HAZ regions. However, this $\gamma$ grain size is still smaller than that observed in the base metal (98 μm), due to the high density of nucleation sites in the large amount of pearlite and the small interlamellar spacing between the $Fe_3C$ precipitates shown in Figure 12. In addition, the pearlitic colonies observed in this region are also significantly larger than those shown in Figures 11(a) and 11(b).

The widths of the primary HAZ microstructural regions, which are measured in the post-weld metallography of the top surface of each weld, are plotted in Figure 13(a). In this figure, the width of the HAZ is defined as the region measured from the fusion zone boundary to the end of the partially transformed region and is shown to increase with increasing input power. Of the three regions, the grain growth region is the widest for all of the input powers and increases in width with increasing power. The fine grain region is the next widest and also increases in width

with increasing power. On the other hand, the partially transformed region displays a constant width across the range of input powers.

These post-weld microstructural features can also be correlated with the high temperature microstructures observed in the SRXRD experiments. The relationship between the high temperature and post-weld microstructures requires knowledge of the kinetics of the $\alpha \rightarrow \gamma$ transformation during heating. Figure 8 shows an example of this correlation for a weld made at an input power of 1984 W. The locations of the fine grain and grain growth regions in the post-weld microstructure are related to the $\gamma$ phase region observed in the SRXRD scans, and the partially transformed region is related to the $\alpha+\gamma$ phase region.

A closer examination of Figure 8 shows that the related high temperature and post-weld regions do not exactly correspond. Differences in the locations of the high temperature and post-weld microstructural regions indicate that the duration of the heating cycle is not of a sufficient length to drive the transformation to its expected level of completion, based on thermodynamic considerations. For example, the $\alpha+\gamma$ region observed in the SRXRD scan is located closer to the fusion zone boundary than the partially transformed region in the post-weld metallography, indicating that the $\alpha \rightarrow \gamma$ transformation has not yet reached completion. With additional heating, the $\alpha \rightarrow \gamma$ transformation can continue to completion within the $\gamma$ region. The existence of ferrite above the A3 temperature shows that the kinetics of the $\alpha \rightarrow \gamma$ transformation trails the heating conditions experienced under these welding conditions and that this transformation requires additional time and temperature to reach completion under these conditions.

In Figure 13(b), the post-weld microstructural measurements are directly compared with the SRXRD measurements and the thermodynamic predictions for the sizes of the $\gamma$ and $\alpha+\gamma$ phase regions. Differences between the metallographic, thermodynamic, and SRXRD measurements of the $\gamma$ phase region are evident, especially at the low input powers where the thermal gradients are the steepest. As the input power is increased, these differences become less pronounced. In fact, at input powers above 2410 W, there is little discernible difference in the measured widths of this region. At these input power levels, the times at the elevated temperatures required to form the $\gamma$ phase are long enough to allow the transformation to reach completion.

In the $\alpha+\gamma$ phase region, the SRXRD measurements are typically larger than both the thermodynamic predictions and metallographic results, which are similar across the range of input

powers. These observations are also consistent with heating occurring at locations following that where the SRXRD scan is taken. Figure 14 shows the progression of the heating cycle at locations near the $\alpha+\gamma$ phase region in the weld made at an input power of 1984 W. This figure shows that the calculated temperatures remain at or above those present where the SRXRD scan is taken. Since the SRXRD scan is not taken at the maximum temperatures experienced in the weld, the $\alpha \rightarrow \gamma$ transformation has not proceeded to its maximum extent in this two phase region. Therefore, as the temperatures continue to rise, the $\alpha \rightarrow \gamma$ transformation continues.

Figure 15 shows a plot comparing the calculated thermal cycle with the SRXRD locations of the $\gamma$ and $\alpha+\gamma$ phase regions for the weld made at an input power of 1984 W. Similar plots have also been made for the welds made at the other input powers. Thermal cycles at x=0 mm and x = ±0.5 mm are shown to account for any potential error in the positioning of the SRXRD scan. Even with this ±0.5 mm variation, differences in the calculated temperatures are only approximately ±10ºC. These similarities in thermal cycles result from the rather small temperature gradients present in the x-direction at these locations.

Using this plot, the temperatures at which the different phase regions exist in the weld can be determined. Table 5 provides a summary of the locations of the boundaries and the corresponding temperatures, along with the level of uncertainty in each of these values, for the primary phase regions at each weld input power. The average temperatures for each of these boundaries are determined from results from all of the input powers and are listed in Table 6. Even though the phase boundary locations differ with changes in the input power, the corresponding temperatures are similar. In general, the values shown in this table display a small level of superheating over the calculated thermodynamic temperatures. For example, in order for the $\alpha \rightarrow \gamma$ transformation to reach completion, a superheat of approximately 60ºC over the calculated A3 temperature is required. These results are consistent with those expected under the rather rapid heating conditions present in these welds.

*Austenite Formation and Homogenization*

The progression of the $\alpha \rightarrow \gamma$ transformation from the formation and growth of austenite through the homogenization of the high temperature austenitic microstructure is directly observed in the SRXRD scan made on each weld. For example, austenite is first formed from the base metal microstructure during heating at temperatures above the calculated A1 temperature.

Figure 16 shows the progress of the transformation as a function of location with respect to the weld centerline for each input power. The austenite volume fractions shown in this figure are based on measurements of the integrated intensities of both the ferrite and austenite peaks present in each diffraction pattern. With changes in the input power, the location of the $\alpha+\gamma$ phase region moves further from the fusion zone boundary, and the austenite volume fractions display a similar sigmoidal distribution.

The rate of change for the austenite volume fractions is also measured at each input power from the sigmoidal fitting of the experimental data. Each set of experimental data is fitted to the following equation:

$$\gamma(wt.\%) = \frac{1}{1 + e^{-\left(\frac{x - x_0}{b}\right)}} \quad (1)$$

where $\gamma$(wt.%) is the measured volume fraction of austenite and b is a measure of the rate of change in the individual curves. Each curve displays a rate of change in the austenite volume fraction between approximately -0.1 and -0.2. Such similarities in the rates of change in austenite can be linked to the thermal cycles experienced in this phase region (See Figure 4(b)). The range of temperatures experienced in this phase region over a distance of approximately 1 mm is similar for all of the welds and can be correlated with heating rates between approximately 50 and 80ºC/sec for the input powers analyzed here. As a result, the $\alpha \rightarrow \gamma$ transformation rate in this phase region is expected to be only minimally affected by the changes in input power.

After the ferrite is transformed to austenite, the SRXRD results begin to show a splitting of the austenite peaks at an average temperature of approximately 861ºC±34ºC over the range of input powers investigated here. This austenite peak splitting persists throughout the majority of the austenite phase field and is characterized primarily by the addition of a diffraction peak at a lower $2\theta$ value and higher d-spacing on each austenite peak present in the diffraction patterns. A similar austenite peak splitting at elevated temperatures has been observed in TRXRD experiments with a 1005 C-Mn steel [36] and in other SRXRD experiments with a 1045 C-Mn steel.[37] The observed peak splitting in this 1045 C-Mn steel indicates that austenite with different lattice parameters exists in the microstructure.

The origin of this peak splitting is related to variations in the composition of the austenite. For example, the effect of changes in the carbon and manganese concentrations on the austenite lattice parameters is well established.[38-40] It is known that increases in the carbon concentration in C-Mn steels result in a pronounced increase in the austenite lattice parameters, independent of the effects of temperature, and in excess of that observed with increases in manganese concentration. For example, the difference between the austenite lattice parameter of pure Fe and an Fe-0.4C alloy at a temperature of 1000ºC can be upwards of 0.01 Å, as compared to the austenite lattice parameter for pure Fe at this same temperature, which is approximately 3.623 Å.[39] The peak shifts observed in the diffraction patterns gathered in the γ phase region in the 1045 C-Mn steel studied here are on the order of 0.3º, which equates to a difference of approximately 0.04 Å in the calculated lattice parameters. A shift in the austenite lattice parameters of this magnitude can be explained by the existence of an austenite phase with carbon concentrations approximately four times the nominal carbon concentration in this steel (0.45%).

Figure 17 shows the changes in the measured austenite lattice parameter with changes in location across the γ and α+γ fields for a weld made at an input power of 1984 W. These measured values are compared with both the calculated thermal cycle for this input power and a set of calculated austenite lattice parameters based on the assumption of a constant coefficient of thermal expansion ($2.1 \times 10^{-5}$/°C), which is typical of that measured in low alloy steels.[41] The measured lattice parameters for the high 2θ austenite peaks (solid circles), which represent the austenite originally transformed from the base metal ferrite, increase with increasing temperatures along a trend similar to that shown for the lattice parameters calculated for a constant thermal expansion.

However, the low 2θ peaks, which appear as part of the peak splitting, show an increasing separation from this trend with increasing temperature. Figure 18 shows that the amount of splitting between these two peaks, which are present in the diffraction patterns obtained from the weld made at an input power of 1984 W, increases until it approaches a maximum value of approximately 0.04 Å at a location 5.2 mm from the weld centerline, which corresponds to a temperature of approximately 1111ºC. Above this temperature, the amount of splitting decreases until none is observed at locations adjacent to the fusion zone and temperatures approaching 1300ºC.

Along with these lattice parameter shifts, changes in the widths of the low 2θ austenite peaks are evident. Figure 19 shows the measured widths of the fcc(111) peaks at each location across the α+γ and γ phase regions for an input power of 1984 W. Similar behavior is also observed at the other input powers. Across the range of temperatures shown in Figure 19, the widths of the high 2θ austenite peaks remain constant, while the width of the low 2θ austenite peaks display a significant broadening, which is not typical with increasing temperatures. Peak broadening such as this is typically attributed to changes in the micro-strain state of the phase being monitored.[29] Such changes in the micro-strain state can be caused by the onset of phase transformations or the diffusion of either substitutional or interstitial alloying elements.

It is clear that there are additional high temperature processes occurring in the austenite phase region. One potential mechanism involves the dissolution of undissolved cementite laths and the subsequent homogenization of the austenite phase.[37] In previous modeling efforts,[10-12] the cementite laths are assumed to be pure $Fe_3C$ and contain only carbon, which diffuses rapidly into the growing austenite under isothermal conditions, thus allowing the cementite to rapidly dissolve. However, this alloy contains an appreciable amount of other alloying elements, namely manganese, which is expected to be concentrated in the cementite phase.[8,13]

Based on these SRXRD observations, the transformation of the base metal microstructure and the homogenization of the resulting austenite phase during welding can thus be broken down into a number of stages. Figure 20 shows a series of schematic diagrams detailing these various stages in the $\alpha \rightarrow \gamma$ transformation occurring across the width of the weld HAZ. In the initial stages (a), ferrite in the pearlite colonies and allotriomorphic ferrite regions which surround them in the base metal microstructure is transformed into austenite ($\gamma_1$) in (b). Because of the rapid heating cycles experienced in the weld HAZ, the cementite laths, which are originally a part of the pearlite colonies, do not completely dissolve before the ferrite in the microstructure is completely consumed at a temperature approaching 827ºC. These cementite laths begin to dissolve with continued heating, introducing C and Mn into the austenite and causing a second, more highly alloyed austenite constituent ($\gamma_2$) to appear, as shown in (c). As the heating continues, these alloying elements, which originated in the cementite laths, continue to diffuse into the less highly alloyed $\gamma_1$ constituent. At temperatures of approximately 1300ºC and above, the chemical composition of the austenite becomes homogenized (d).

The splitting in the austenite peaks, which is first observed near a temperature of 861ºC, signals the appearance of the second austenite constituent ($\gamma_2$). This $\gamma_2$ constituent appears at a lower 2θ value than $\gamma_1$ and thus exhibits a larger lattice parameter. Figures 21(a) through 21(c) show the progression of the splitting at locations between 6.4 mm and 5.2 mm from the weld centerline for the weld made with an input power of 1984 W. Initially, the split between the $\gamma_1$ and $\gamma_2$ peaks is rather small, since $\gamma_2$ first begins to form from the $\gamma_1$ located within the pearlite colonies. With increasing temperatures, the amount of peak splitting increases as both the carbon and manganese from the cementite diffuse into the $\gamma_2$ constituent. A summary of the locations and corresponding temperatures where this maximum splitting is observed in each weld is included in Table 5. When considering all of the welds made here, the amount of peak splitting reaches a maximum at an average temperature of 1115ºC, as listed in Table 6. This temperature is assumed to correspond to the completion of the cementite dissolution.

The amount of $\gamma_2$ present in the microstructure should correspond closely to the amount of pearlite present in the base metal, which was measured to be 88% at room temperature. At the completion of the cementite dissolution, the austenitic microstructure should contain nearly this same amount of $\gamma_2$, while the amount of $\gamma_1$ should be equal to the amount of allotriomorphic ferrite (12%). An examination of the peak area measurements has been made, and an example of the variation in the fraction of $\gamma_2$ in the austenitic microstructure is shown in Figure 22. For an input power of 1984 W, the fraction of $\gamma_2$ in the austenitic microstructure reaches a maximum value of approximately 75% at a location 5.0 mm from the weld centerline. This value is consistent with the amount of $\gamma_2$ that would be expected to form from the pearlite.

At the highest temperatures encountered in the weld HAZ, the low 2θ peak lattice parameter curve in Figure 17 decreases in lattice parameter, and the widths of the low 2θ austenite peaks in Figure 19 narrow. The combination of these two observations indicates that the chemical composition of the austenitic microstructure is homogenizing. With further increases in temperature, the amount of splitting decreases until only a single peak is observed at locations near the fusion zone boundary, indicating that the two sets of peaks have joined. At the locations approaching the fusion zone boundary, the homogenization of the austenite phase (γ) reaches completion as the diffusion of the alloying elements has created a single chemically homogenous austenite phase.

The SRXRD results indicate that γ is homogenizing at temperatures of approximately 1300ºC in a few seconds. This observation can be tested using a rather simple one-dimensional diffusion calculation to estimate the distances that the carbon and manganese alloying elements diffuse at these times and temperatures:

$$x = 2\sqrt{Dt} \tag{2}$$

where x is the diffusion distance (cm), D is the diffusivity ($cm^2$/sec), and t is the time (sec). The diffusivity of carbon in austenite is based on the following Arrhenius relationship:

$$D = Ae^{\frac{-Q}{RT}} \tag{3}$$

where A is the frequency factor, Q is the activation energy, R is the ideal gas constant, and T is the temperature. Values for A (0.08 $cm^2$/sec) and Q (132.3 kJ/mol) are taken from a standard reference for a 0.4 wt.% C steel.[34] The calculated diffusion distance at temperatures approaching 1340ºC is approximately 20 μm for a time of 1 sec.

Similar calculations for the diffusion of manganese in austenite have been made. In these calculations, values for A (1.25 $cm^2$/sec) and Q (256.2 kJ/mol) are also taken from a standard reference.[34] The calculated diffusion distance of manganese at this same elevated temperature (1340ºC) is approximately 0.23 μm for a time of 1 sec. Over this same short time frame, which is typical of welding conditions, the manganese diffusion distance is two orders of magnitude lower than that for carbon.

In order for the austenitic microstructure to homogenize, these alloying elements must diffuse from the $\gamma_2$ constituent to the $\gamma_1$ constituent. The $\gamma_2$ constituent, in which the C and Mn are concentrated, encompasses the pearlitic regions observed in the base metal, and the $\gamma_1$ constituent exists in the regions where allotriomorphic ferrite is observed in the base metal. The width of the $\gamma_1$ constituent, based on measurements of the base metal allotriomorphic ferrite region, is only 20 μm on average. Therefore, the C and Mn must diffuse, on average, a minimum of 10 μm to drive the homogenization of the austenite phase to completion.

Whereas the diffusion distance of carbon is in line with the size of the $\gamma_1$ constituent regions, the manganese diffusion distance is not. It can be concluded that only the carbon is homogenizing throughout the austenitic microstructure and that manganese, given its small diffusion distance, is not. The resulting high temperature austenitic microstructure will therefore have areas of high and low manganese content, as defined by the $\gamma_1$ and $\gamma_2$ constituent regions but a relatively uniform carbon content. Since manganese has a rather minimal effect on the resulting austenite lattice parameters, particularly in comparison to that of carbon [40], the non-homogenous distribution of manganese does not contribute to an observable splitting or recombining of the austenite diffraction peaks, like that which occurs with variations in the carbon concentration.

The mechanism described above is based on observations from the weld made at an input power of 1984 W. These observations are also consistent with those made at the other input powers analyzed here. An analysis of the average values for the temperatures at which the austenite peak splitting is observed in the various welds (Table 6) shows that the difference in observed temperatures is rather minimal. It is therefore apparent that there is little or no effect of changes in power input on the mechanisms governing the formation and homogenization of the austenite phase during welding.

These results also provide further insight into the mechanisms driving the $\alpha \rightarrow \gamma$ phase transformation during the rapid heating cycles experienced in welding. Previous models [1-9] have typically considered the dissolution of cementite to occur instantaneously during the $\alpha \rightarrow \gamma$ phase transformation under isothermal annealing conditions. The addition of the carbon from the cementite drives the $\alpha \rightarrow \gamma$ phase transformation to completion in the former pearlite regions before the transformation reaches completion in the allotriomorphic ferrite. As a result, two austenite constituents are formed during the transformation.

In the observations presented here, though, the cementite, under rapid weld heating conditions, exists at temperatures well above the A3 temperature. Since the cementite laths do not completely dissolve during the $\alpha \rightarrow \gamma$ phase transformation, only a single austenite constituent is present, along with the undissolved cementite laths, at the completion of the $\alpha \rightarrow \gamma$ transformation. The second austenite constituent does not appear until the cementite dissolves at elevated temperatures. It is thus clear, that the rapid heating cycles experienced during welding have a pronounced effect on the mechanism of the $\alpha \rightarrow \gamma$ phase transformation and the homogenization of the austenite phase by delaying the dissolution of the cementite laths.

The SRXRD observations discussed here are more in line with the conclusions of another model which takes into account the important role of cementite dissolution in the $\alpha \rightarrow \gamma$ phase transformation.[10-12] In this model, the dissolution of cementite takes a finite period of time and occurs at the same time as the transformation of ferrite to austenite. In turn, the kinetics of the transformation can be affected, depending on the heating or isothermal conditions under which the transformation is occurring. Additional work [8,13-14] which documents the existence of cementite at temperatures above the A3 temperature also supports the presence of cementite at the elevated temperatures present during welding along with the observation that the complete dissolution of cementite does not coincide with the $\alpha \rightarrow \gamma$ phase transformation. The SRXRD results presented here also go further than these previous studies by tying the dissolution of cementite to the homogenization of the austenite phase at elevated temperatures under welding conditions.

## Summary and Conclusions

SRXRD scans are performed on GTA welds with input powers ranging from 1000 W to 3750 W on AISI 1045 C-Mn steel. Four prominent phase regions are observed in each weld: the liquid phase corresponding to the weld fusion zone and three solid phase regions, comprised of the austenite, the two phase austenite and ferrite, and the ferrite phase fields. These results are then combined with temperatures calculated from a coupled thermo-fluids mathematical model in order to track the progress of the $\alpha \rightarrow \gamma$ phase transformation at the peak of the heating cycle. The resulting high temperature microstructure along with several important calculated isotherms are then compared with post-weld microstructures. Based on these results, the following conclusions can be made:

- Changes in the weld input power produce variations in the the size of the austenite phase region measured in the SRXRD scans. However, even with a greater than 3x difference in input powers, the size of the $\alpha+\gamma$ phase region in each weld remains unchanged along the x=0 mm path.
- Measurements of the ferrite phase fractions in the $\alpha+\gamma$ phase regions in each SRXRD scan show a similar sigmoidal decrease in $\gamma$ with increasing distance from the weld

centerline for each input power. This similarity is attributed to the similar thermal cycles experienced across the locations where this phase region exists.

- By comparing the SRXRD results taken near the peak of the heating cycle with the calculated temperatures and the resulting HAZ post-weld microstructures for each input power, the kinetics of the $\alpha \rightarrow \gamma$ transformation under a range of welding conditions are examined. In the SRXRD scans, ferrite is observed at locations and temperatures above the calculated A3 temperatures. The superheat required to transform $\alpha$ to $\gamma$ is on the order of approximately 60ºC.

- The formation and homogenization of austenite is directly observed in real time during typical weld heating cycles. Analysis of these data shows that the process begins with the transformation of the ferrite in the base metal pearlite and allotriomorphic ferrite to form a single austenite constituent. The dissolution of the cementite laths, which exists as part of the pearlite colonies in the base metal microstructure, is observed at temperatures of approximately 884ºC, which is well above the A3 temperature for this alloy. As these laths dissolve, a second highly alloyed austenite constituent appears. This second austenite constituent exists until the temperatures increase to levels above approximately 1300ºC, at which time carbon diffuses throughout the $\gamma$ grains to form a chemically homogenous austenitic phase.

- In each SRXRD scan, a splitting of the austenite peaks in the $\gamma$ phase region is observed. The size of this region increases with increasing input power, and the splitting is observed over a range of calculated temperatures between approximately 860ºC and 1290ºC. The low $2\theta$ austenite peaks, corresponding to the highly alloyed austenite constituent, display significant peak broadening at these same locations. By the end of the heating cycle, the splitting of the austenite peaks is no longer visible.

- In these SRXRD experiments, the role that the dissolution of the cementite lathes plays in the formation and homogenization of austenite under welding conditions is described. These results support the conclusions of models [10-12] which take into account the prominent role of cementite dissolution in the $\alpha \rightarrow \gamma$ transformation.

With this more complete picture of the $\alpha \rightarrow \gamma$ phase transformation during welding, a more in-depth examination of the kinetics of this transformation can be pursued and more accurate kinetic models can be developed. This study also provides a baseline for future work aimed at examining the effects of changes in carbon concentration in real time on the kinetics of the $\alpha \rightarrow \gamma$ phase transformation.

## Acknowledgements

This work has been performed under the auspices of the U.S. Department of Energy, by the University of California, Lawrence Livermore National Laboratory under Contract No. W-7405-ENG-48. Portions of this research were carried out at the Stanford Synchrotron Radiation Laboratory, a national user facility operated by Stanford University on behalf of the U.S. Department of Energy, Office of Basic Energy Sciences. The authors would also like to thank Prof. T. DebRoy at The Pennsylvania State University for providing us the use of the transient heat transfer and fluid flow code for the calculation of weld thermal cycles. Other thanks go to Mr. A.T. Teruya (LLNL) for writing the LabView® software used in the control of the welding experiments and Mr. R. Vallier (LLNL) for preparation of the metallographic samples.

## References

1. G.R. Speich, V.A. Demarest, and R.L. Miller: *Metall. Trans. A*, 1981, vol. 12A, pp. 1419-1428.

2. A. Jacot, M. Rappaz, and R.C. Reed: *Acta Mater.*, 1998, vol. 46(11), pp. 3949-3962.

3. A. Jacot and M. Rappaz: *Acta. Mater.*, 1997, vol. 45(2), pp. 575-585.

4. A. Jacot and M. Rappaz: *Acta Mater.*, 1998, vol. 47(5), pp. 1645-1651.

5. C. Atkinson, T. Akbay, and R.C. Reed: *Acta Metall Mater.*, 1995, vol. 43(5), pp. 2013-2031.

6. D. Gaude-Fugarolas and H.K.D.H. Bhadeshia: *J. Mater. Sci.*, 2003, vol. 38, pp. 1195-1201.

7. F.G. Caballero, C. Capdevila, D. San Martín, and C. García De Andrés: in *Austenite Formation and Decomposition*, ed. E.B. Damm and M. Merwin, ISS/TMS, Warrendale, PA, 2003, pp. 457-474.

8. C.R. Brooks: *Principles of the Austenitization of Steels*, Kluwer Academic Publishers, Dordrecht, 1992.

9. S. Estay, L. Chengji, and G.R. Purdy: *Canad Metall Quarter.*, 1984, vol. 23(1), pp. 121-130.

10. R.C. Reed, T. Akbay, Z. Shen, J.M. Robinson, and J.H. Root: *Mater. Sci. Eng. A*, 1998, vol. 256, pp. 152-165.

11. T. Akbay, R.C. Reed, and C. Atkinson: *Acta Metall. Mater.*, 1994, vol. 47(4), pp. 1469-1480.

12. Z. Shen, T. Akbay, J.P. Bourne, and R.C. Reed: in *Trends in Welding Research*, ed. H.B. Smartt, J.A. Johnson, and S.A. David, ASM International Materials Park, OH, 1996, pp. 217-222.

13. M. Hillert, K. Nilsson, and L.-E. Törndahl: *J. Iron Steel Instit.*, 1971, vol. 209, pp. 49-66.

14. M. Nemoto: *Metall. Trans. A*, 1977, vol. 8A, pp. 431-437.

15. K. Easterling: *Introduction to the Physical Metallurgy of Welding*, 2nd Ed., Butterworth-Heinemann, Oxford, 1992.

16. S. Kou: *Welding Metallurgy*, 2nd Ed., Wiley-Interscience, Hoboken, NJ, 2003.

17. J.W. Elmer, T.A. Palmer, and S.S. Babu: *Adv. Mater Process*, 2002, vol. 160(11), pp. 23-26.

18. J.W. Elmer, J. Wong, and T. Ressler: *Metall. Mater. Trans. A*, 1998, vol. 29A, pp. 2761-2773.

19. Z. Yang, J.W. Elmer, J. Wong, and T. DebRoy: *Weld J.*, 2000, vol. 79(4), pp. 97s–111s.

20. J.W. Elmer, J. Wong, and T. Ressler: *Metall. Mater. Trans. A*, 2001, vol. 32A, pp. 1175-1188.

21. J.W. Elmer, J. Wong, and T. Ressler: *Scripta Mater*, 2000, vol. 43(8), pp. 751-757

22. T.A. Palmer, J.W. Elmer, and J. Wong: *Sci. Tech. Weld. Join.*, 2002, vol. 7(3), pp. 159-171.

23. J. W. Elmer, T. A. Palmer, W. Zhang, B. Wood, and T. DebRoy: *Acta Mater.*, 2003, vol. 51, pp. 3333-3349.

24. W. Zhang, J.W. Elmer, and T. DebRoy: *Scripta Mater*, 2002, vol. 46, pp. 753-757.

25. W. Zhang, J.W. Elmer, and T. DebRoy: *Mater Sci Eng A*, 2002, vol. 333(1-2), pp. 320-335.

26. J.W. Elmer, T.A. Palmer, and J. Wong: *J. Appl. Phys.*, 2003, vol. 93(4), pp. 1941-1947.

27. J.W. Elmer, T.A. Palmer, S.S. Babu, W. Zhang, and T. DebRoy: *Weld. J.*, 2004, vol. 83(9), pp. 244s-253s.

28. V. Karpenko, J.H. Kinney, S. Kulkarni, K. Neufeld, C. Poppe, K.G. Tirsell, J. Wong, J. Cerino, T. Troxel, J. Yang, E. Hoyer, M. Green, D. Humpries, S. Marks, and D. Plate: *Rev. Sci. Instrum.*, 1989, vol. 60, pp. 1451-1460

29. B.D. Cullity and S.R. Stock: *Elements of X-Ray Diffraction*, 3rd Edition, Prentice Hall, Upper Saddle River, NJ, 2001.

30. S.A. David and T. DebRoy: *Science*, 1992, vol. 257, pp. 497-502.

31. T. DebRoy and S.A. David: *Rev. Mod. Phys*, 1995, vol. 67(1), pp. 85-112.

32. K. Mundra, T. DebRoy, and K.M. Kelkar: *Numer. Heat Trans. A*, 1996, vol. 29, pp. 115-129.

33. Z. Yang and T. DebRoy: *Metall. Mater. Trans. B*, 1999, vol. 30B, pp. 483-493.

34. E.A. Brandes, ed.: *Smithells Metals Reference Book*, 7th Edition, London: Butterworth and Heinemann, 1992.

35. M.W. Chase, Jr., C.A. Davies, J.R. Downey, Jr., D.J. Frurip, R.A. Mcdonald, and A.N. Syverud: *JANAF Thermochemical Tables*, 3rd Edition, American Chemical Society and American institute for Physics, Washington, DC, 1985.

36. J. Wong, T. Ressler, and J.W. Elmer: *J. Synchrotron Rad.*, 2003, vol. 10, pp. 154-167.

37. T.A. Palmer and J.W. Elmer: *Scripta Mater.*, 2005, vol. 53, pp. 535-540.

38. L. Cheng, A. Böttger, T.H. de Keijser, and E.J. Mittemeijer: *Scripta Metall. Mater.*, 1990, vol. 24, pp. 509-514.

39. M. Onink, C.M. Brakman, F.D Tichelaar, E.J. Mittemeijer, S. van der Zwaag, J.H. Root, and N.B. Konyer: *Scripta Metall. Mater.*, 1993, vol. 29, pp. 1011-1016.

40. D.J. Dyson and B. Holmes: *J. Iron Steel Inst.*, 1970, vol. 208, pp. 469-474.

41. S.S. Babu, Private Communication, 2005.

## List of Tables

## List of Figures

Figure 15. Plot comparing the calculated thermal cycles with the locations at which the three primary phase regions are observed in the SRXRD scans for the weld made at an input power of 1984 W. Thermal cycles at x=0 mm, x=0.5 mm, and x=-0.5 mm are shown to account for any potential error in the placement of the SRXRD linear scan.

Figure 16. Plot showing variation in measured austenite fractions in the $\alpha+\gamma$ phase regions measured in the welds made at each power setting.

Figure 17. Plot showing variations in the lattice parameters for the ferrite and austenite phases across the length of SRXRD scan for the weld made at an input power of 1984 W. The corresponding thermal cycle is also shown.

Figure 18. Plot showing the magnitude of the peak splitting in the austenite peaks measured in the $\gamma$ phase regions as a function of distance from the center of the weld for the weld made at an input power of 1984 W.

Figure 19. Plot showing variations in the FWHM values for the fcc(111) and bcc(110) peaks across the range of locations for the SRXRD scan from the weld made at an input power of 1984 W. The corresponding thermal cycle is also included.

Figure 20. Schematic diagrams showing (a) the progression of the $\alpha \rightarrow \gamma$ transformation from the as-received base metal through (b) the transformation of the microstructure to austenite ($\gamma_1$) to (c) the dissolution of the cementite laths and the formation of a second austenite constitutent ($\gamma_2$) to (d) the homogenization of the austenite ($\gamma$).

Figure 21(a-c). Plots of x-ray diffraction patterns taken during the SRXRD run at an input power of 1984 W showing the evolution of the splitting of the fcc(111) peak at locations of (a) y= 6.4 mm, (b) y = 5.6 mm, and (c) y = 5.2 mm.

Figure 22. Plot showing the amount of the $\gamma_2$ constituent measured in the $\gamma$ phase regions as a function of distance from the center of the weld for the weld made at an input power of 1984 W.

Table 1. Summary of Experimental Welding Parameters.

| Peak Current (A) | Background Current (A) | Average Current (A) | Voltage (V) | Power (W) |
|---|---|---|---|---|
| 59 | 41 | 50 | 20.0 | 1003 |
| 89 | 62 | 76 | 17.5 | 1289 |
| 117 | 82 | 99 | 15.7 | 1561 |
| 146 | 102 | 124 | 16.0 | 1984 |
| 175 | 123 | 149 | 16.2 | 2410 |
| 204 | 143 | 174 | 17.3 | 3002 |
| 234 | 164 | 199 | 18.9 | 3759 |

Table 2. Summary of material parameters used in heat transfer modeling of weld pool size and shape.

| | |
|---|---|
| **Density of Liquid (gm/cm$^3$)** | 7.87 |
| **Effective Viscosity of Liquid (gm/cm-sec)** | 0.75 |
| **Solidus Temperature (K)** | 1694 |
| **Liquidus Temperature (K)** | 1767 |
| **Enthalpy of Solid at Melting Point (cal/gm)** | 251 |
| **Enthalpy of Liquid at Melting Point (cal/gm)** | 315.5 |
| **Specific Heat of Solid (cal/gm-K)** | 0.095 |
| **Specific Heat of Liquid (cal/gm-K)** | 0.3 |
| **Thermal Conductivity of Solid (cal/cm-sec-K)** | 0.1 |
| **Effective Thermal Conductivity of Liquid (cal/cm-sec-K)** | 0.215 |
| **Coefficient of Thermal Expansion (1/K)** | $1.0 \times 10^{-5}$ |
| **d(gamma)/dT of pure material (dynes/cm-K)** | -0.155 |
| **Concentration of Surface Active Species (wt%)** | 0.020 |
| **Surface Excess at Saturation (mole/cm$^2$)** | $1.3 \times 10^{-9}$ |
| **Enthalpy of Segregation (cal/mole)** | $-3.97 \times 10^{4}$ |
| **Entropy Factor** | $3.2 \times 10^{-3}$ |

Table 3. Arc radii and arc efficiencies used in the calculations of the weld pool size and shape.

| | **1003 W** | **1289 W** | **1561 W** | **1984 W** | **2410 W** | **3002 W** | **3759 W** |
|---|---|---|---|---|---|---|---|
| **Arc Current (A)** | 50.15 | 73.65 | 99.45 | 124 | 148.75 | 173.5 | 198.9 |
| **Arc Voltage (V)** | 20 | 17.5 | 15.7 | 16 | 16.2 | 17.3 | 18.9 |
| **Arc Efficiency** | 0.90 | 0.84 | 0.92 | 0.80 | 0.75 | 0.83 | 0.70 |
| **Arc Radius (mm)** | 0.145 | 0.145 | 0.200 | 0.185 | 0.250 | 0.365 | 0.400 |
| **Preheat Temperature (ºC)** | 260 | 260 | 260 | 280 | 300 | 310 | 305 |

Table 4. Summary of Experimental and Modeled Weld Pool Sizes.

| Power (W) | Weld Width (mm) | | Weld Depth (mm) | | Aspect Ratio | | Modeled Peak Temperature (ºC) |
|---|---|---|---|---|---|---|---|
| | Measured | Modeled | Measured | Modeled | Measured | Modeled | |
| 1003 | 5.24 | 5.55 | 2.83 | 2.85 | 0.54 | 0.51 | 1862 |
| 1289 | 6.13 | 6.08 | 4.05 | 3.81 | 0.66 | 0.63 | 1920 |
| 1561 | 7.80 | 7.76 | 4.77 | 4.52 | 0.61 | 0.58 | 1878 |
| 1984 | 7.81 | 7.96 | 5.85 | 5.77 | 0.75 | 0.72 | 1938 |
| 2410 | 9.37 | 9.52 | 5.64 | 5.79 | 0.60 | 0.61 | 1851 |
| 3002 | 11.81 | 12.52 | 6.50 | 6.80 | 0.55 | 0.54 | 1810 |
| 3759 | 12.99 | 13.20 | 6.47 | 6.82 | 0.50 | 0.52 | 1818 |

Table 5. Temperatures corresponding with observations of austenite peak splitting and two phase ferrite and austenite regions in each weld.

| | 1003 W | | 1289 W | | 1561 W | | 1984 W | | 2410 W | | 3002 W | | 3759 W | |
|---|---|---|---|---|---|---|---|---|---|---|---|---|---|---|
| | Begin | End | Begin | End | Begin | End | Begin | End | Begin | End | Begin | End | Begin | End |
| *Austenite Region* | | | | | | | | | | | | | | |
| Location (mm) | 4.4 | 3 | 5.2 | 3.4 | 6 | 3.8 | 6.6 | 3.8 | 8.2 | 4.6 | 10.2 | 6.2 | 10.4 | 6.4 |
| Temperature (ºC) | 930 | 1337 | 875 | 1297 | 906 | 1434 | 878 | 1448 | 802 | 1436 | 804 | 1422 | 837 | 1435 |
| *Austenite Splitting* | | | | | | | | | | | | | | |
| Location (mm) | 4.8 | 3.4 | 5.4 | 4 | 6 | 3.8 | 6.6 | 4.2 | 8.2 | 5.4 | 9.8 | 7 | 10 | 6.6 |
| Temperature (ºC) | 860 | 1195 | 844 | 1116 | 906 | 1434 | 878 | 1357 | 802 | 1267 | 850 | 1281 | 884 | 1420 |
| *Maximum Splitting* | | | | | | | | | | | | | | |
| Location (mm) | 4.0 | --- | 4.2 | --- | 4.6 | --- | 5.2 | --- | 6.6 | --- | 7.8 | --- | 7.6 | --- |
| Temperature (ºC) | 1020 | --- | 1065 | --- | 1206 | --- | 1111 | --- | 1025 | --- | 1138 | --- | 1243 | --- |
| $\alpha+\gamma$ *Region* | | | | | | | | | | | | | | |
| Location (mm) | 5.6 | 4.6 | 6.4 | 5.4 | 7 | 6.2 | 7.6 | 6.8 | 9.6 | 8.4 | 11.2 | 10.4 | 11.8 | 10.6 |
| Temperature (ºC) | 706 | 845 | 728 | 844 | 771 | 878 | 765 | 851 | 674 | 779 | 707 | 783 | 698 | 814 |

Table 6. Summary of average temperatures corresponding with observations of the austenite phase region, austenite peak splitting, and two phase ferrite and austenite regions in each weld.

| | **Austenite Phase Region** | | **Austenite Peak Splitting** | | | **Ferrite + Austenite Phase Region** | |
|---|---|---|---|---|---|---|---|
| | **Begin** | **End** | **Begin** | **End** | **Maximum Splitting** | **Begin** | **End** |
| ***Average (°C)*** | 862 | 1401 | 861 | 1293 | 1115 | 721 | 827 |
| ***Standard Deviation (°C)*** | 49 | 59 | 34 | 118 | 86 | 36 | 37 |

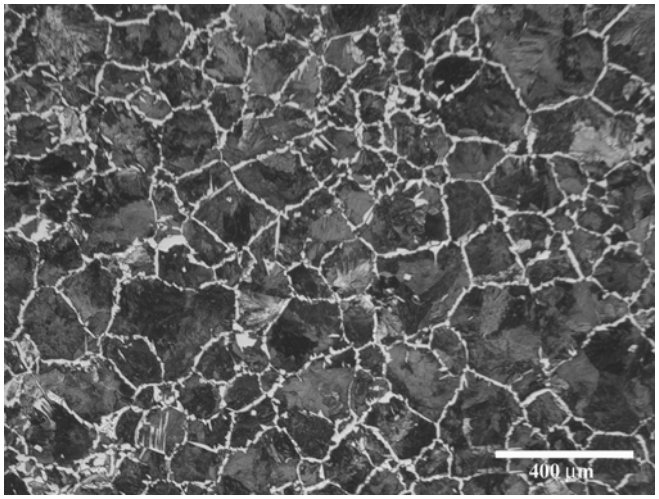


(a)

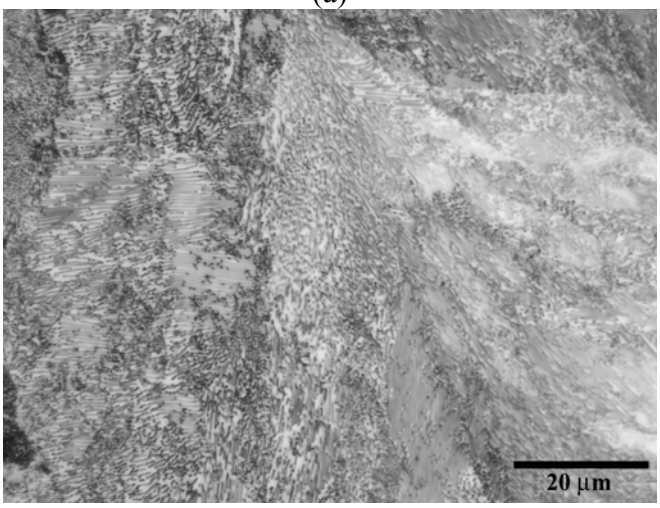


(b)


(c)

Figure 1(a-c). Micrographs showing the base metal microstructure typical of the AISI 1045 C-Mn steel samples used in this study.

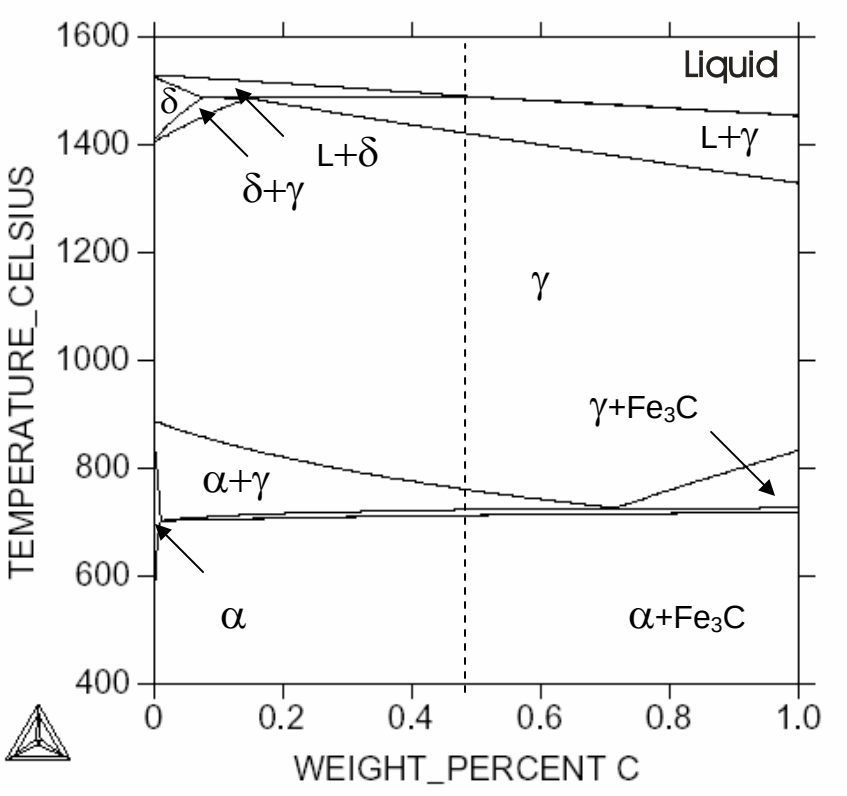


Figure 2. Calculated pseudobinary phase diagram for the AISI 1045 steel. The nominal carbon concentration of the alloy is indicated as the vertical dashed line.

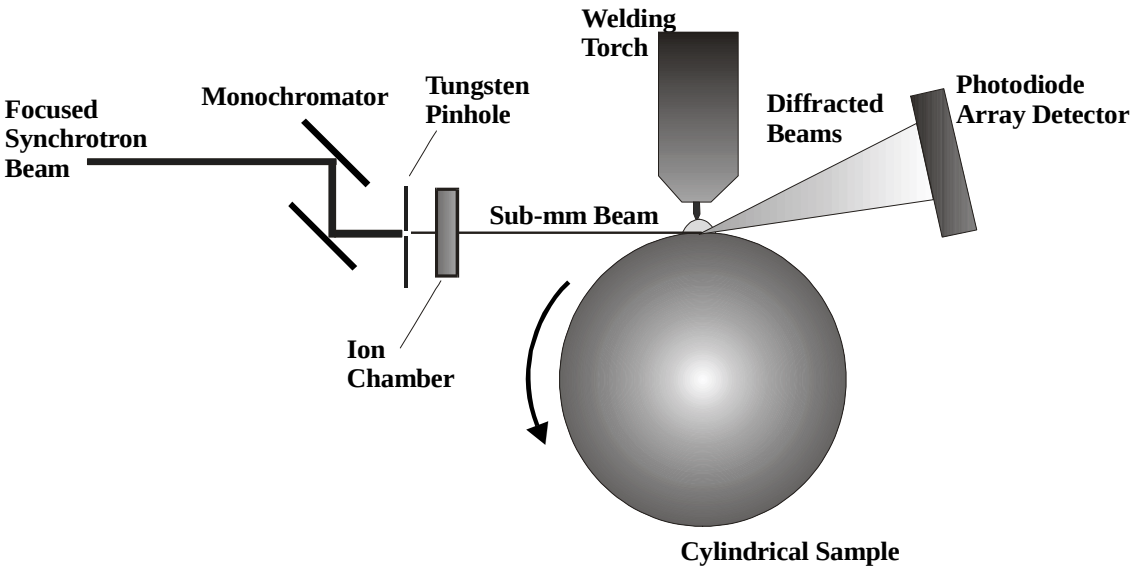


Figure 3. Schematic diagram showing experimental set-up for SRXRD experiments.

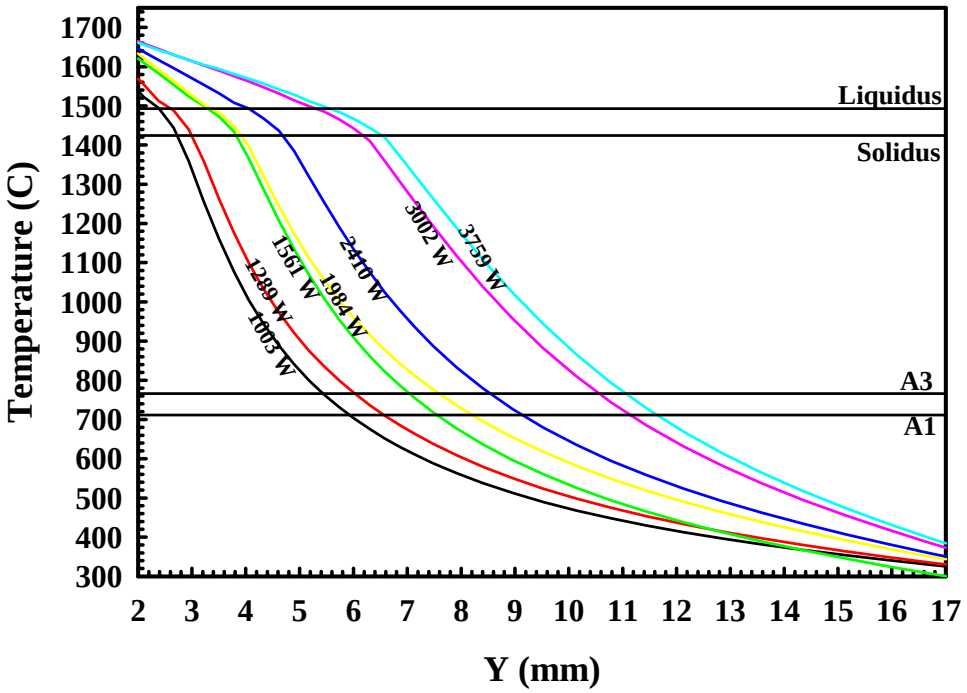


(a)

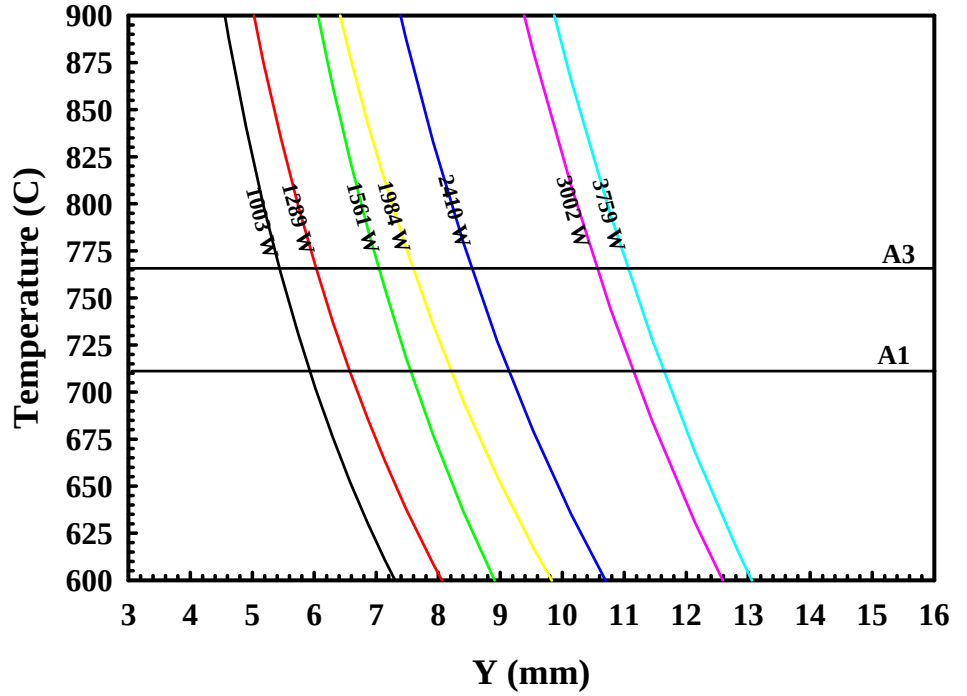


(b)

Figure 4(a&b). Plots showing the calculated temperatures experienced (a) along the entire range of the SRXRD scans and (b) at temperatures in the vicinity of the A1 and A3 temperatures for each weld input power.

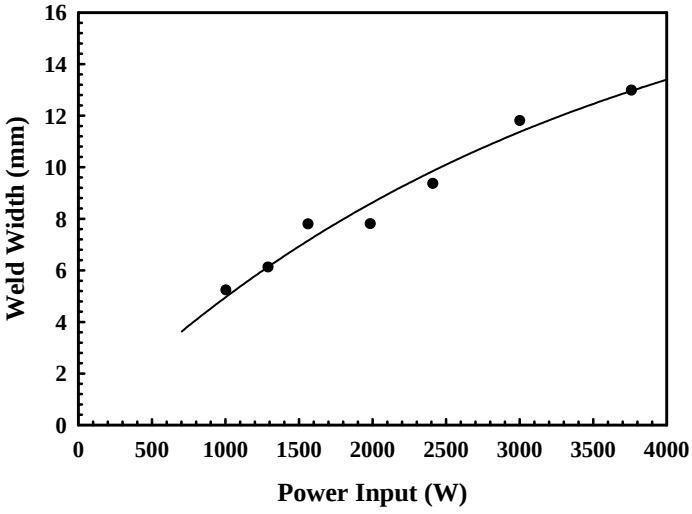


(a)

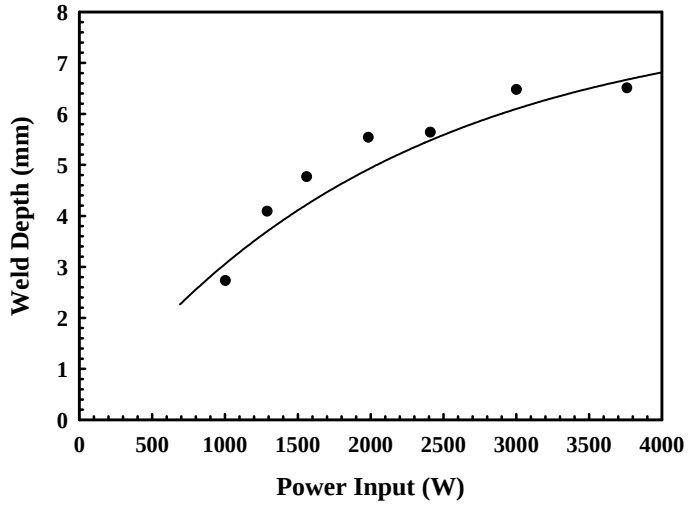


(b)

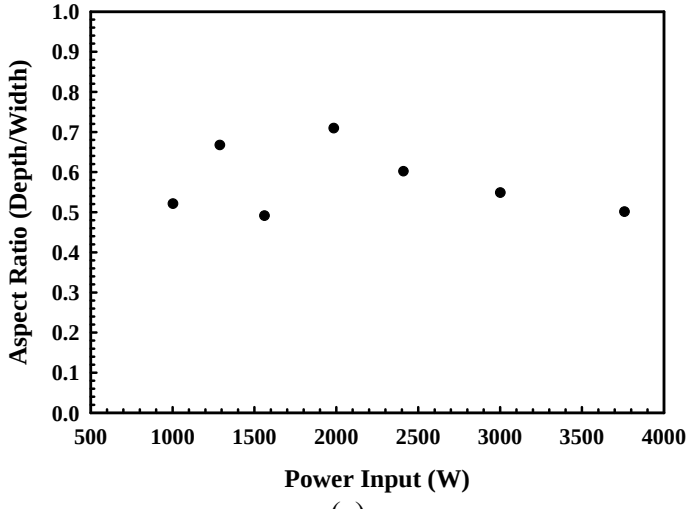


(c)

Figure 5(a-c). Comparison between measured weld (a) width, (b) depth, and (c) aspect ratio (depth/wdith) as a function of input power.

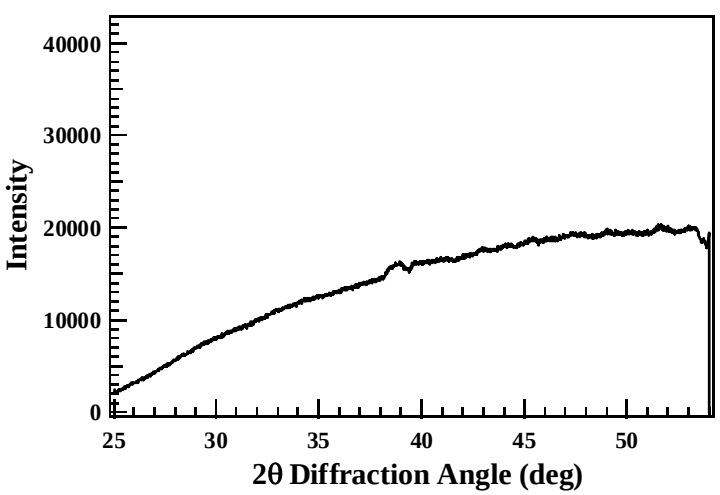


(a)

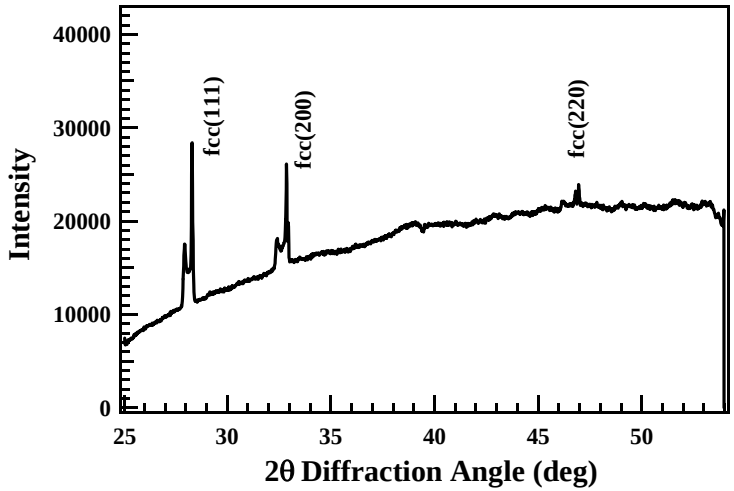


(b)

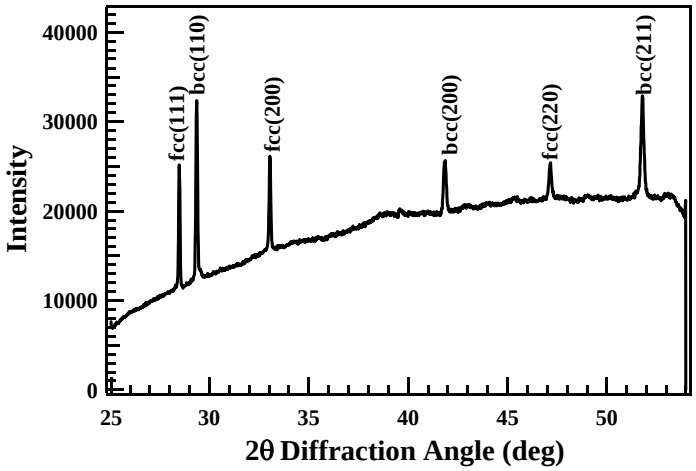


(c)

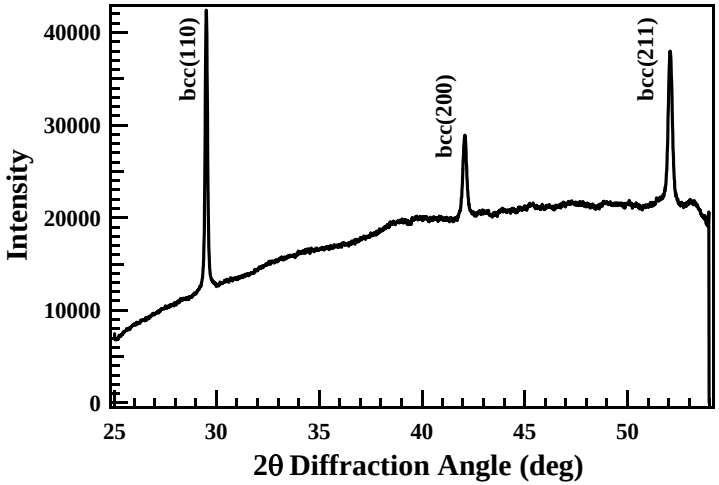


(d)

Figure 6(a-d). Plots of x-ray diffraction patterns taken during the SRXRD run made at an input power of 1984 W showing (a) the liquid phase (y=3.2 mm), (b) austenite peaks in the γ phase region (y=5.4 mm), (c) ferrite and austenite peaks in the α + γ region (y=7.4 mm) and (d) ferrite peaks in the ferrite phase region (y=11.6 mm).

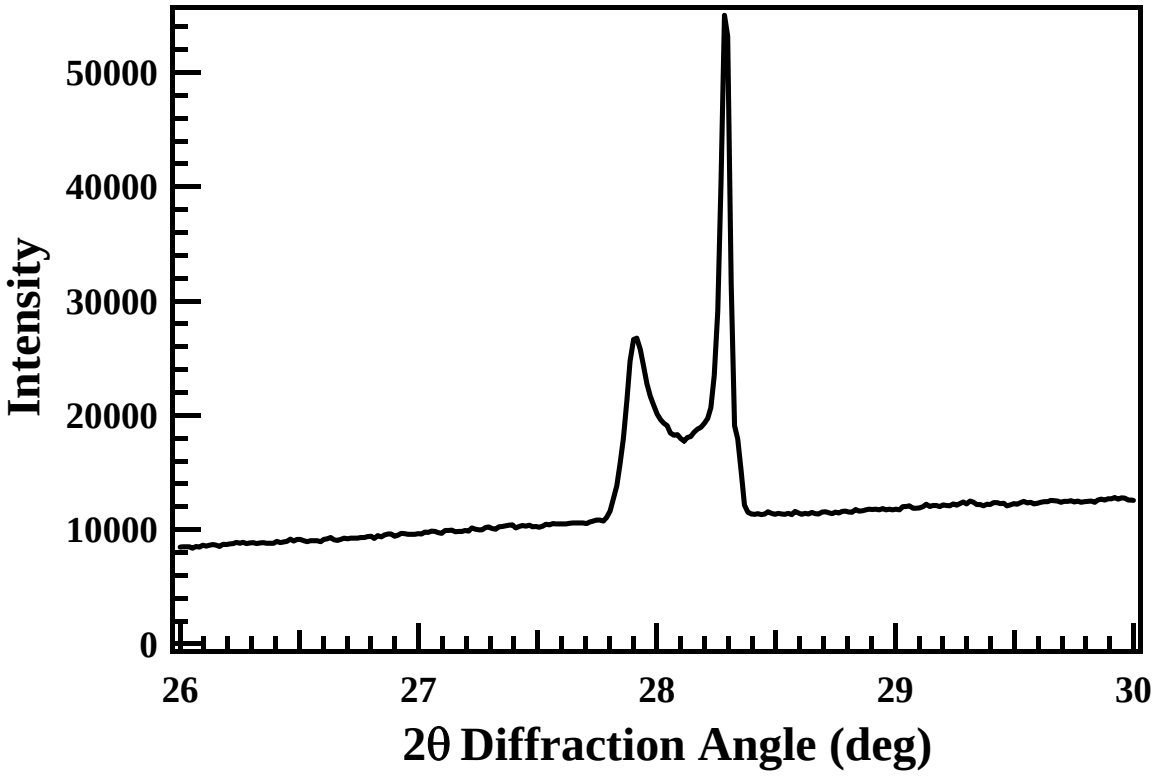


Figure 7. A plot of an x-ray diffraction pattern taken during an SRXRD run showing a typical example of the splitting observed in an fcc(111) austenite peak taken at y = 5.2 mm.

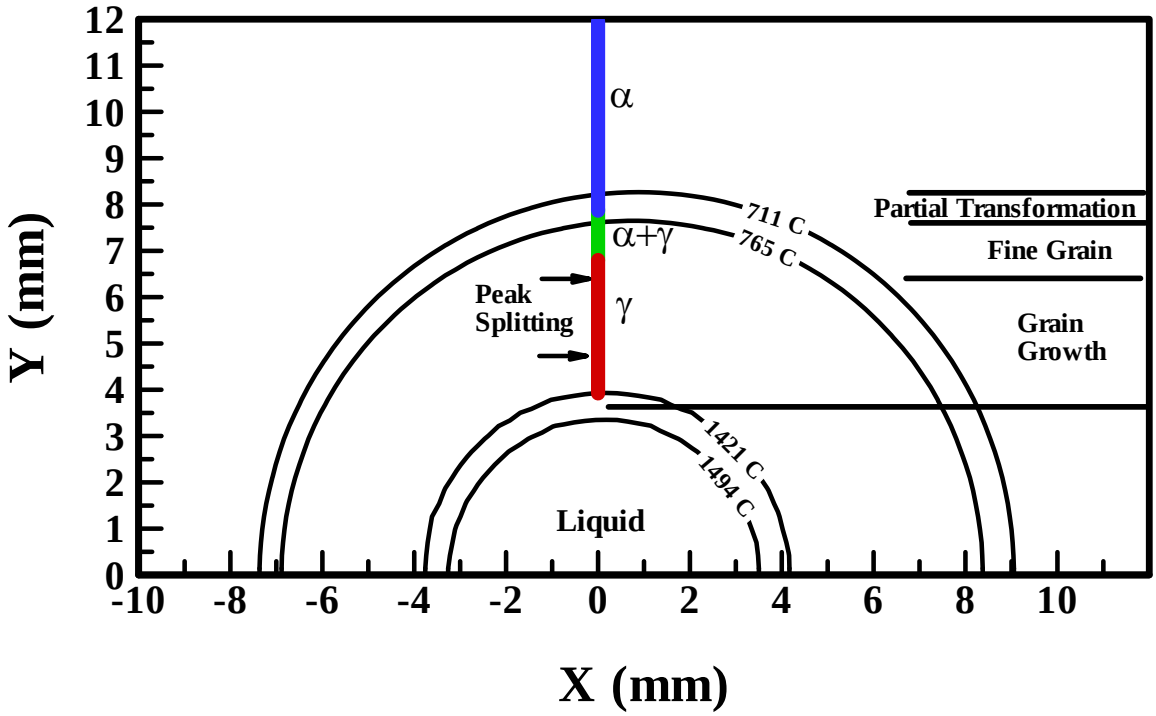


Figure 8. Plot showing the combination of calculated isotherms, SRXRD experimental observations, and the widths of the HAZ microstructural regions observed in the post-weld metallography for the weld made at an input power of 1984 W. The calculated isotherms correspond to the liquidus (1494ºC), solidus (1421ºC), A3 temperature (765ºC), and the A1 temperature (711ºC).

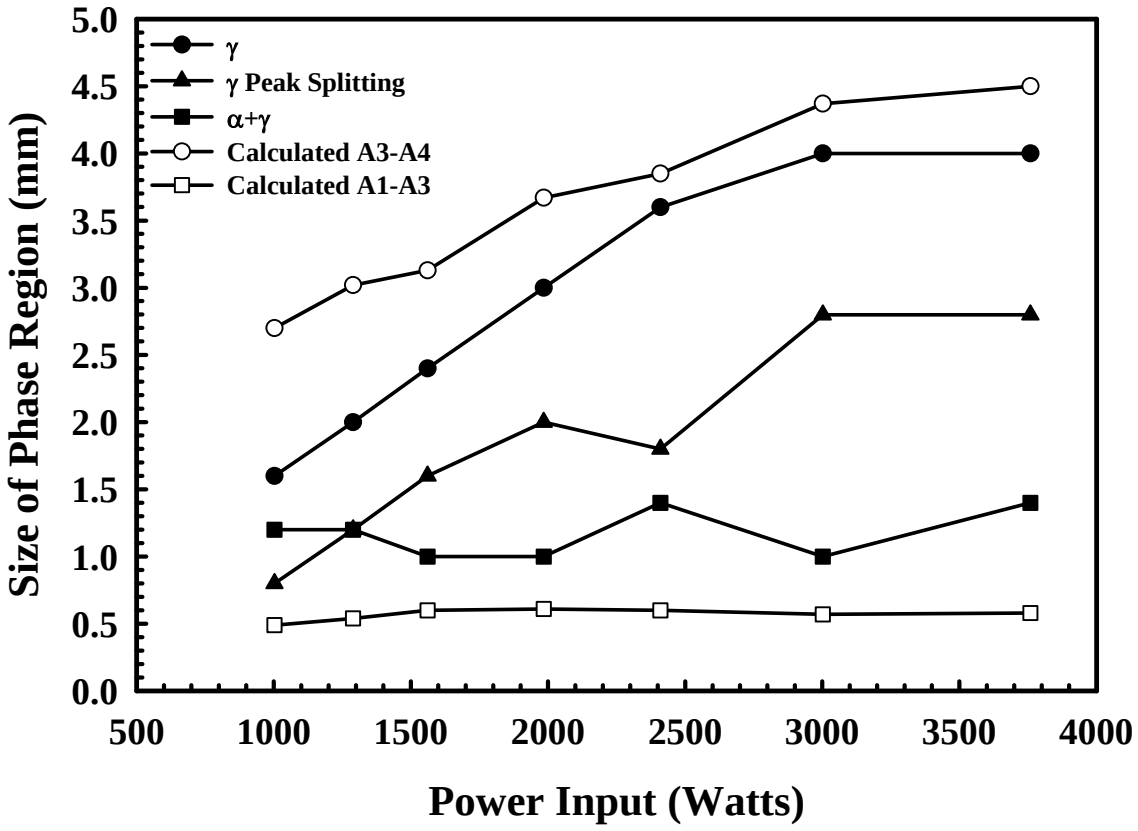


Figure 9. Comparison between the sizes of the primary phase regions measured in the HAZ of each weld during the SRXRD experiments and those calculated at the equilibrium transformation temperatures. In addition to the sizes of the austenite and α+γ phase regions, the size of a prominent peak splitting region in the austenite phase region is also noted.

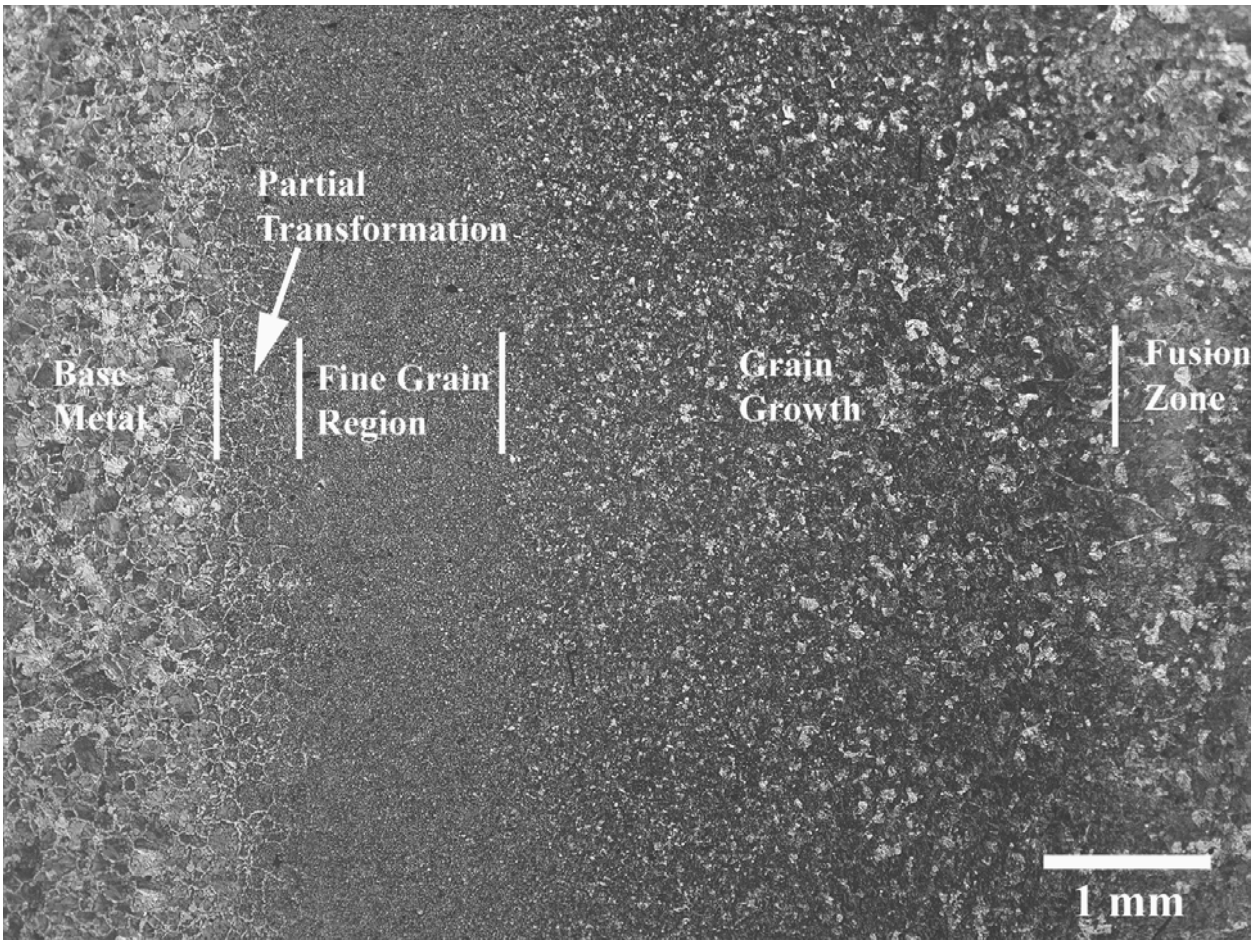


Figure 10. Micrograph showing an overall view of the top surface of the weld HAZ made at an input power of 1984 W.

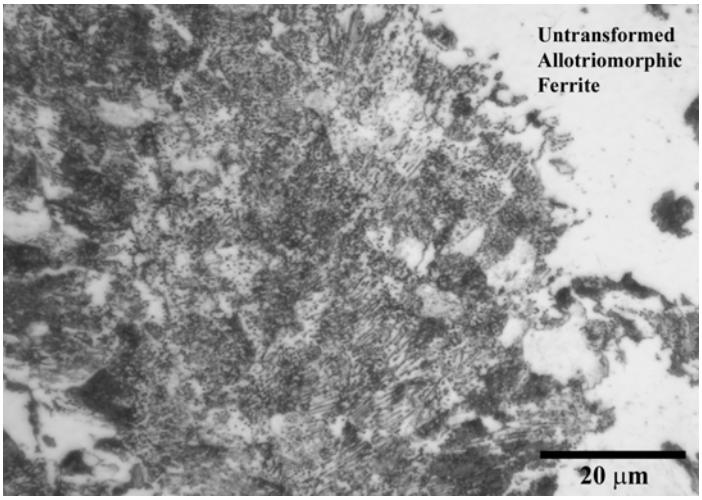


(a)

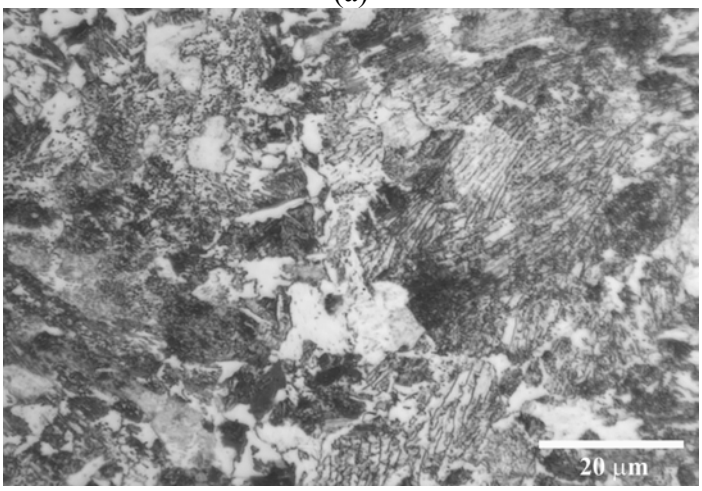


(b)

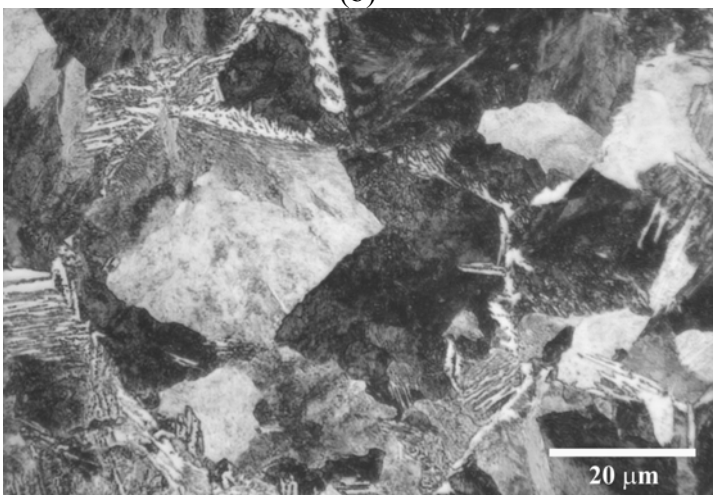


(c)

Figure 11(a-c). Micrographs showing higher magnification images of (a) the partially transformed region, (b) the fine grain region, and (c) the grain growth region on the top surface of the weld HAZ made at an input power of 1984 W.

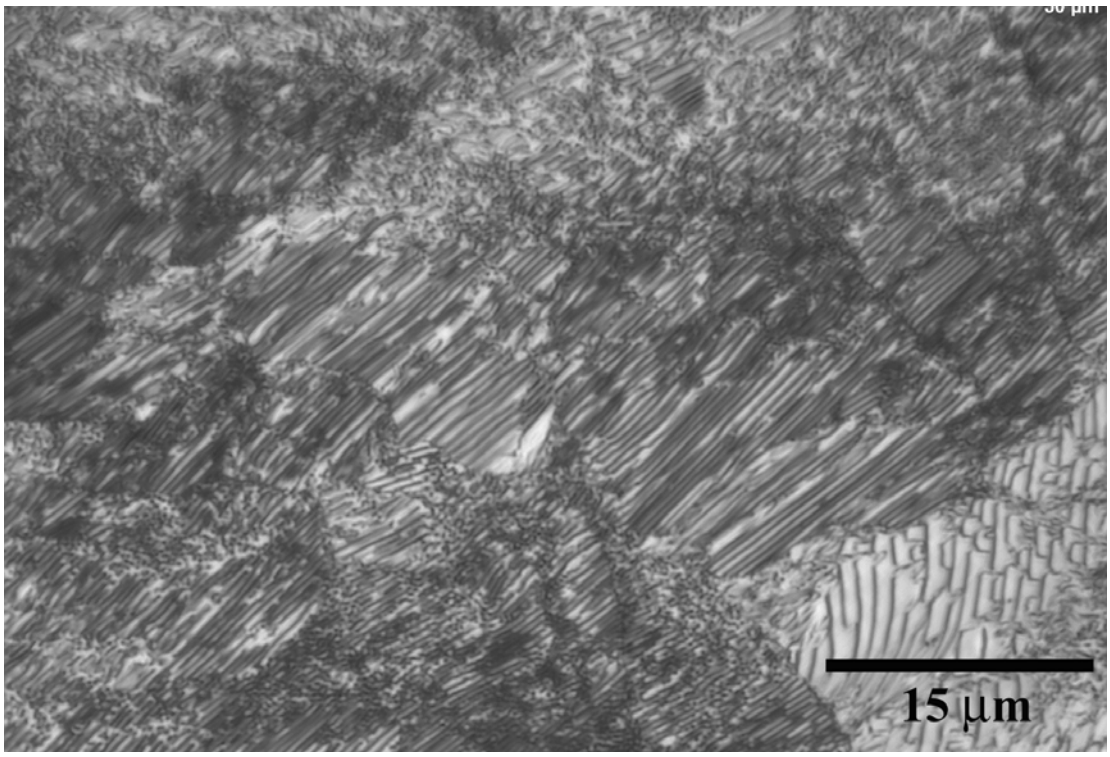


Figure 12. Micrograph showing the small interlamellar spacing present between the $Fe_3C$ precipitates in the pearlite regions of the base metal microstructure.

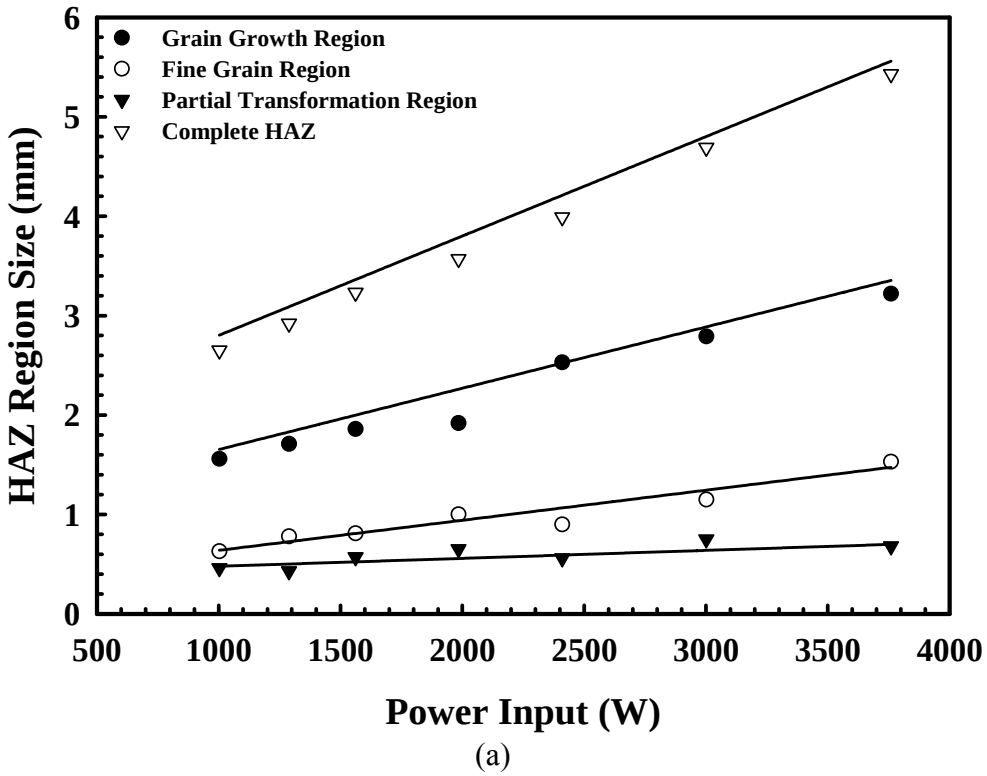


(a)

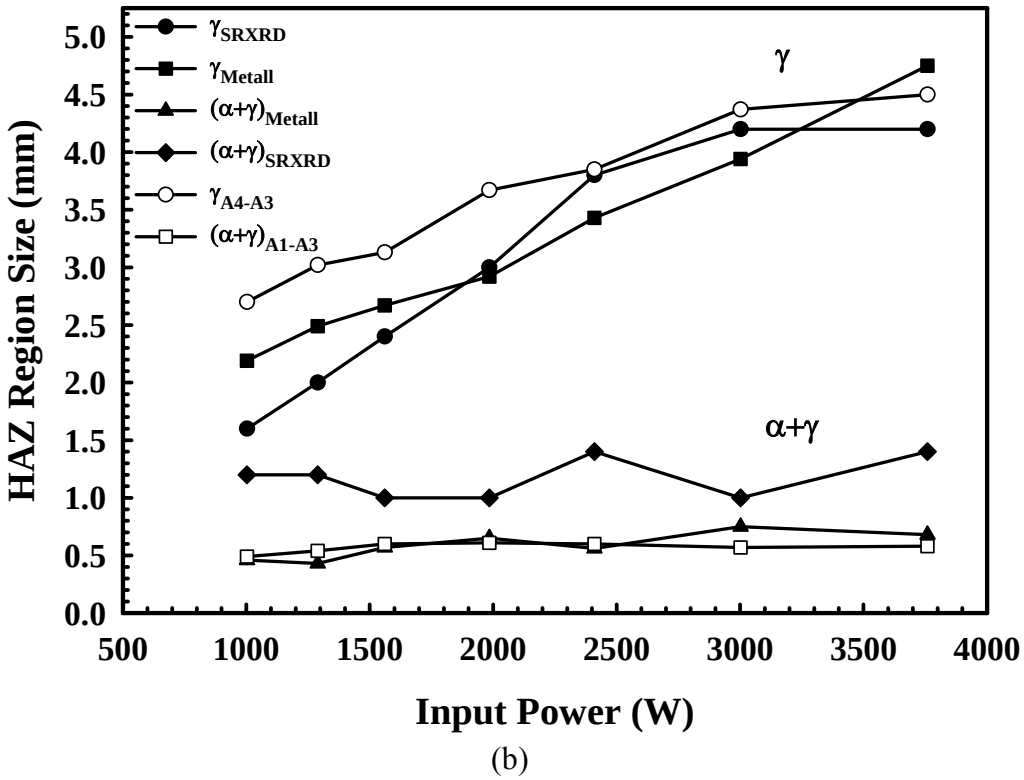


(b)

Figure 13(a&b). Plots showing (a) variations in the sizes of the HAZ microstructural regions measured metallographically as a function of the input power and (b) a comparison between the metallographic and SRXRD experimental results and thermodynamic calculations for the γ and α+γ phase regions.

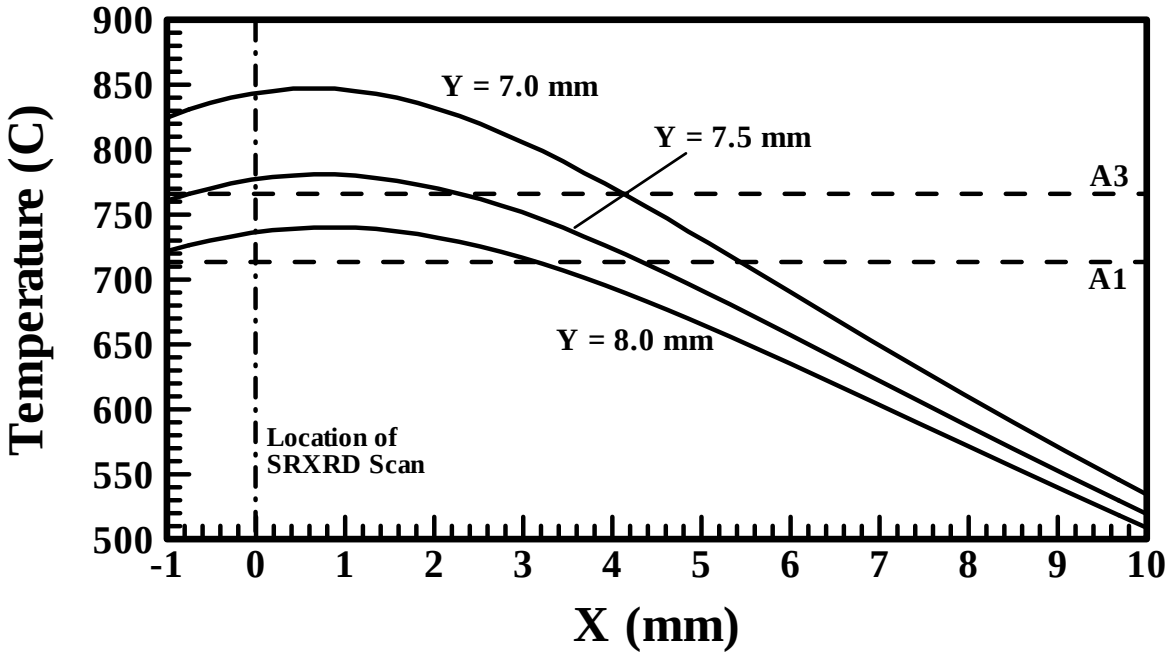


Figure 14. Plot showing the calculated thermal cycles parallel to the weld direction at three locations (Y = 7.0, 7.5, and 8.0 mm) for the weld made at an input power of 1984 W. These thermal cycles show that heating continues at locations following that where the SRXRD scan is made (X = 0 mm).

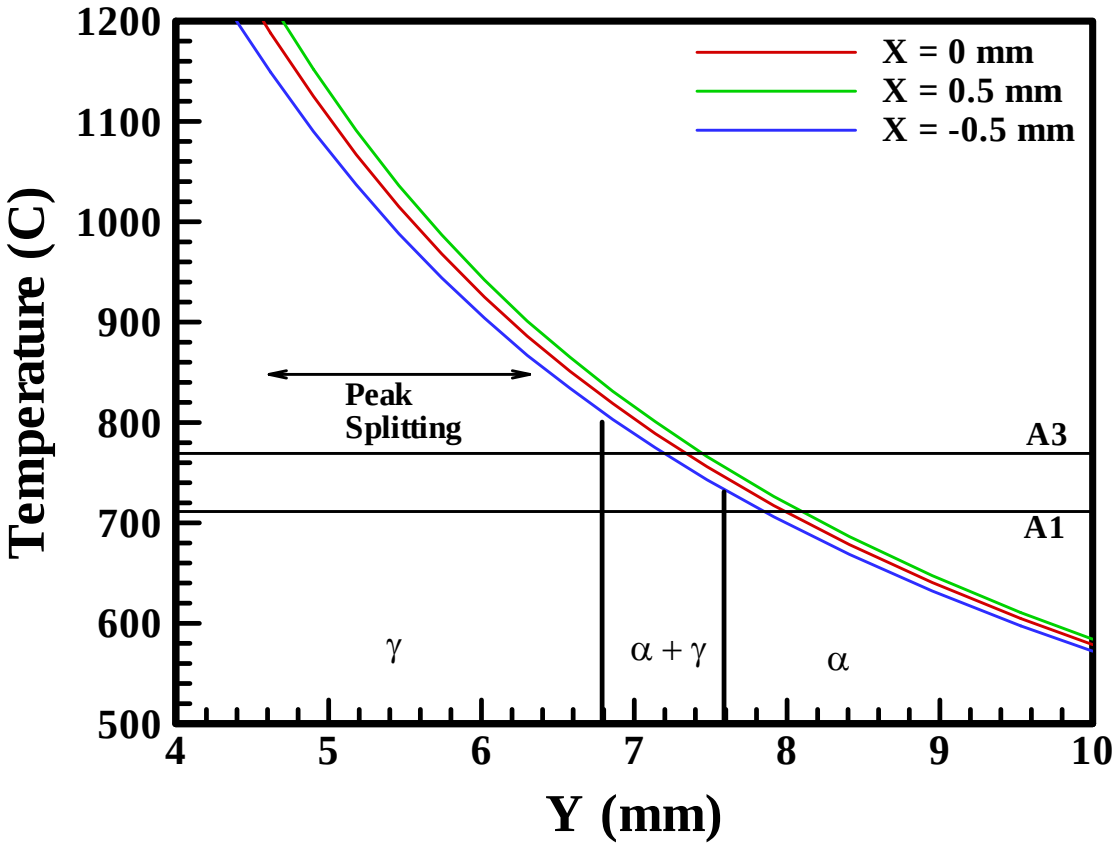


Figure 15. Plot comparing the calculated thermal cycles with the locations at which the three primary phase regions are observed in the SRXRD scans for the weld made at an input power of 1984 W. Thermal cycles at x=0 mm, x=0.5 mm, and x=-0.5 mm are shown to account for any potential error in the placement of the SRXRD linear scan.

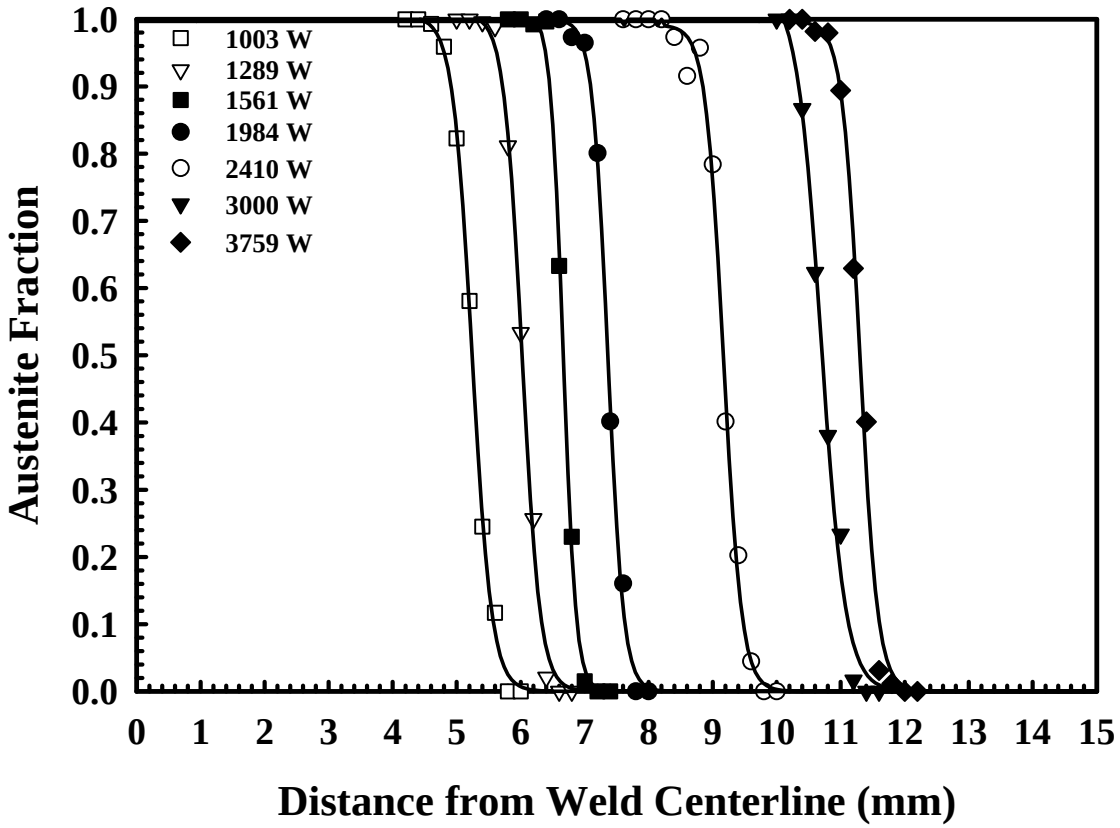


Figure 16. Plot showing variation in measured austenite fractions in the α+γ phase regions measured in the welds made at each power setting.

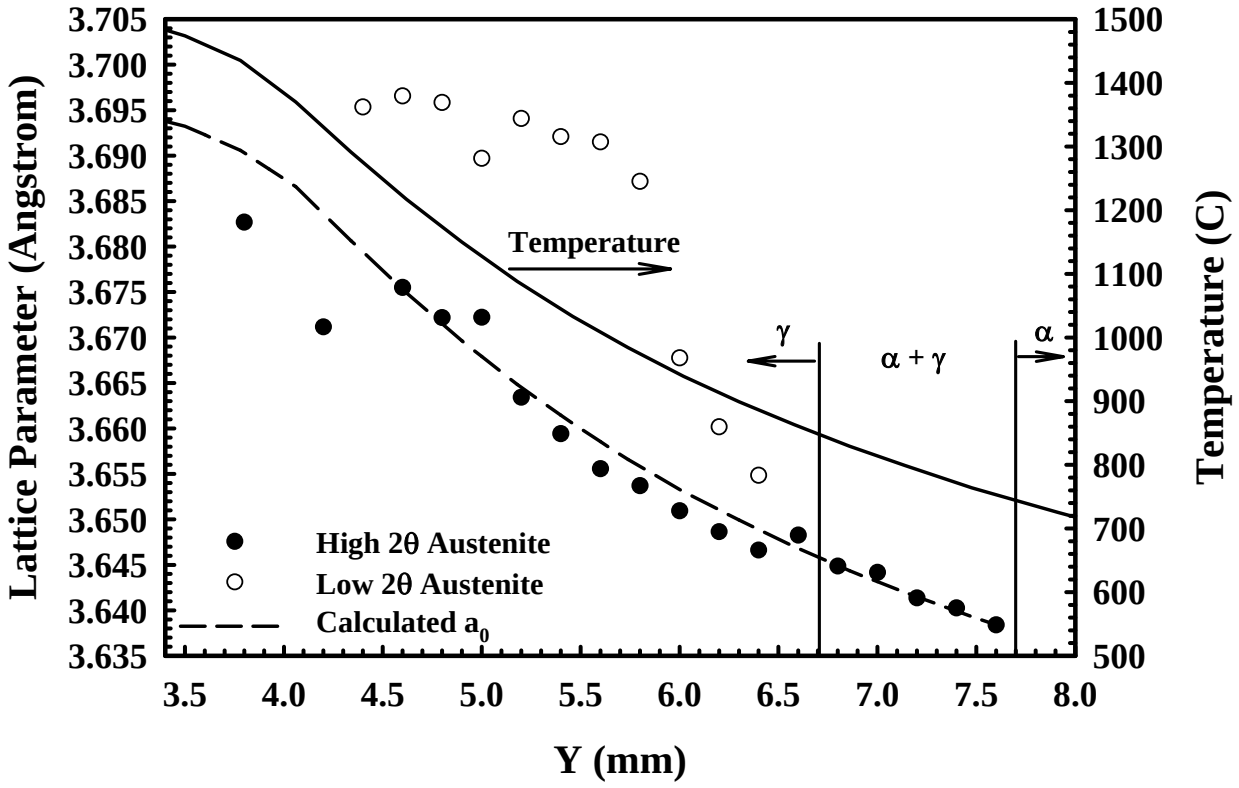


Figure 17. Plot showing variations in the lattice parameters for the ferrite and austenite phases across the length of SRXRD scan for the weld made at an input power of 1984 W. The corresponding thermal cycle is also shown.

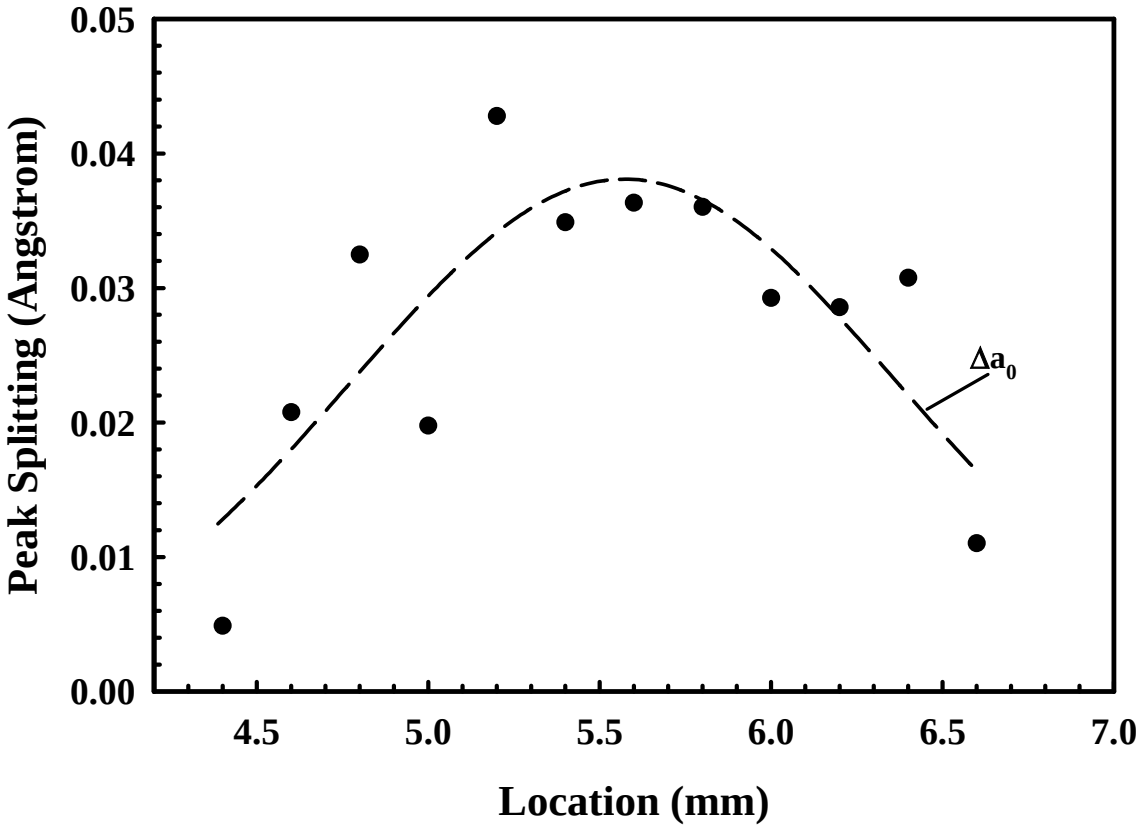


Figure 18. Plot showing the magnitude of the peak splitting in the austenite peaks measured in the γ phase regions as a function of distance from the center of the weld for the weld made at an input power of 1984 W.

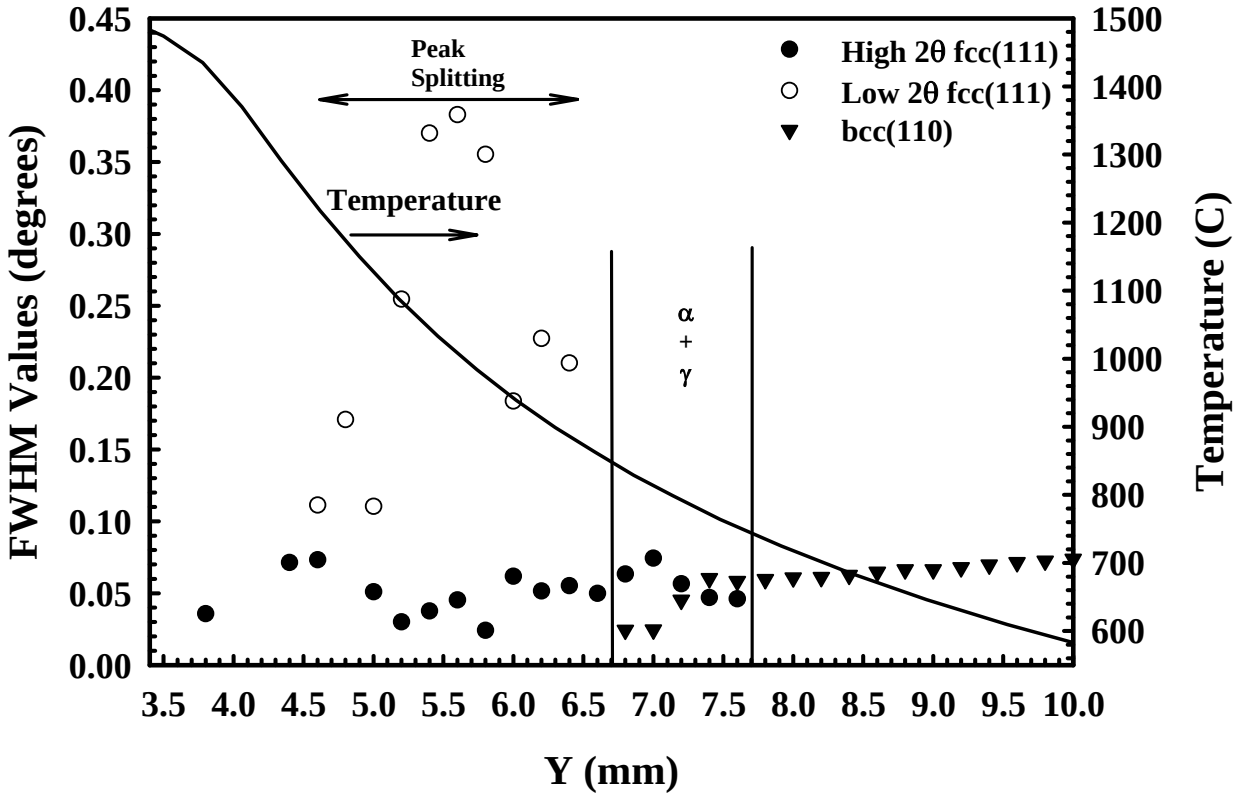


Figure 19. Plot showing variations in the FWHM values for the fcc(111) and bcc(110) peaks across the range of locations for the SRXRD scan from the weld made at an input power of 1984 W. The corresponding thermal cycle is also included.

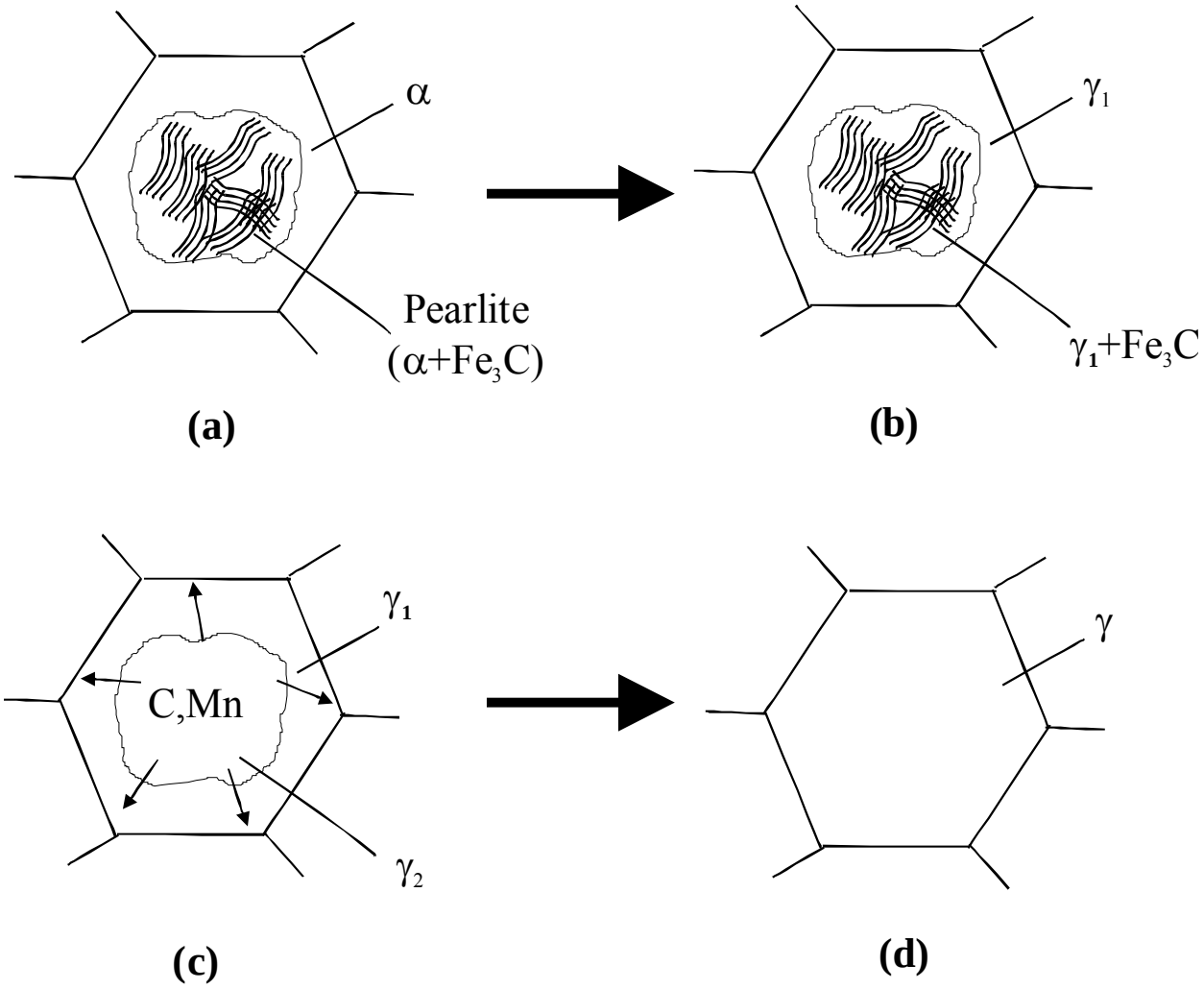


Figure 20. Schematic diagrams showing (a) the progression of the $\alpha \rightarrow \gamma$ transformation from the as-received base metal through (b) the transformation of the microstructure to austenite ($\gamma_1$) to (c) the dissolution of the cementite laths and the formation of a second austenite constitutent ($\gamma_2$) to (d) the homogenization of the austenite ($\gamma$).

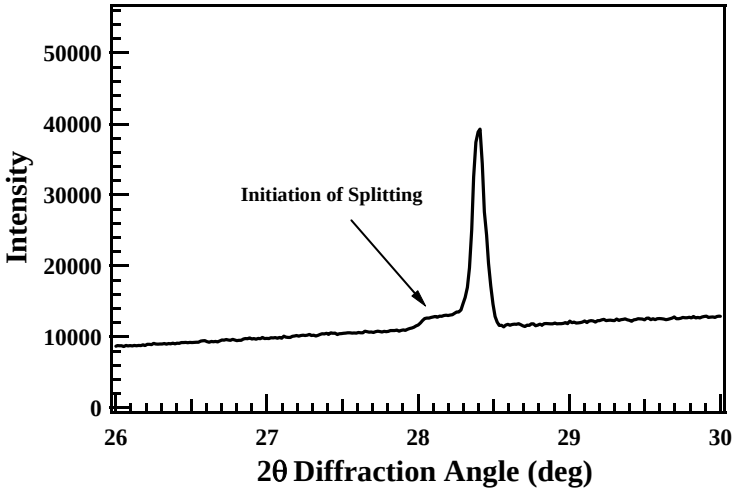


(a)

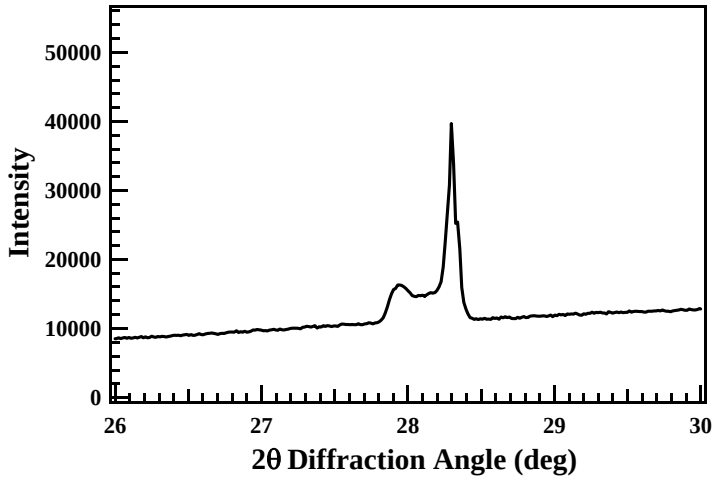


(b)

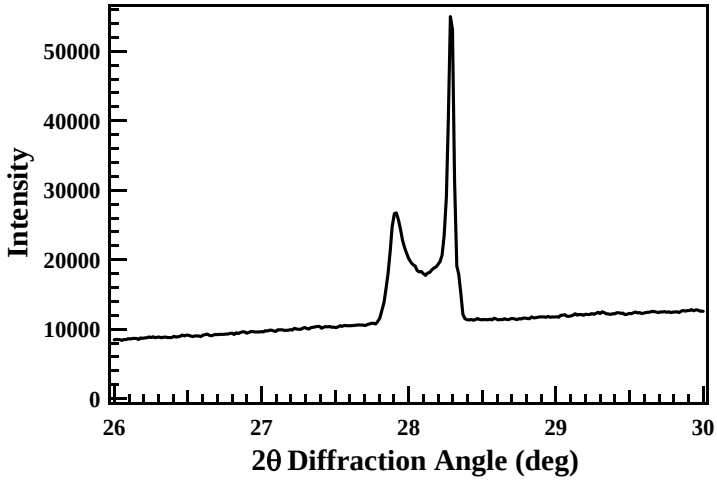


(c)

Figure 21(a-c). Plots of x-ray diffraction patterns taken during the SRXRD run at an input power of 1984 W showing the evolution of the splitting of the fcc(111) peak at locations of (a) y= 6.4 mm, (b) y = 5.6 mm, and (c) y = 5.2 mm.

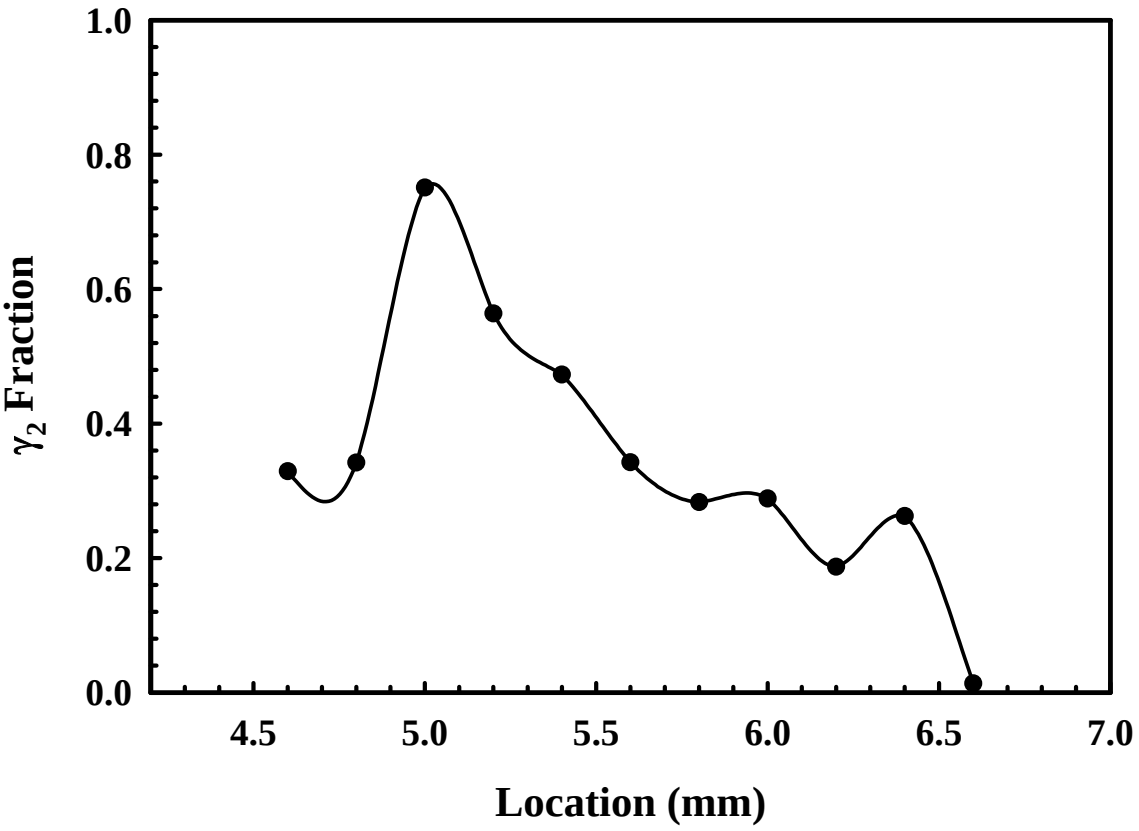


Figure 22. Plot showing the amount of the $\gamma_2$ constituent measured in the $\gamma$ phase regions as a function of distance from the center of the weld for the weld made at an input power of 1984 W.